Molecular Cell

Article

Stress-induced nuclear condensation of NELF drives transcriptional downregulation

Graphical Abstract

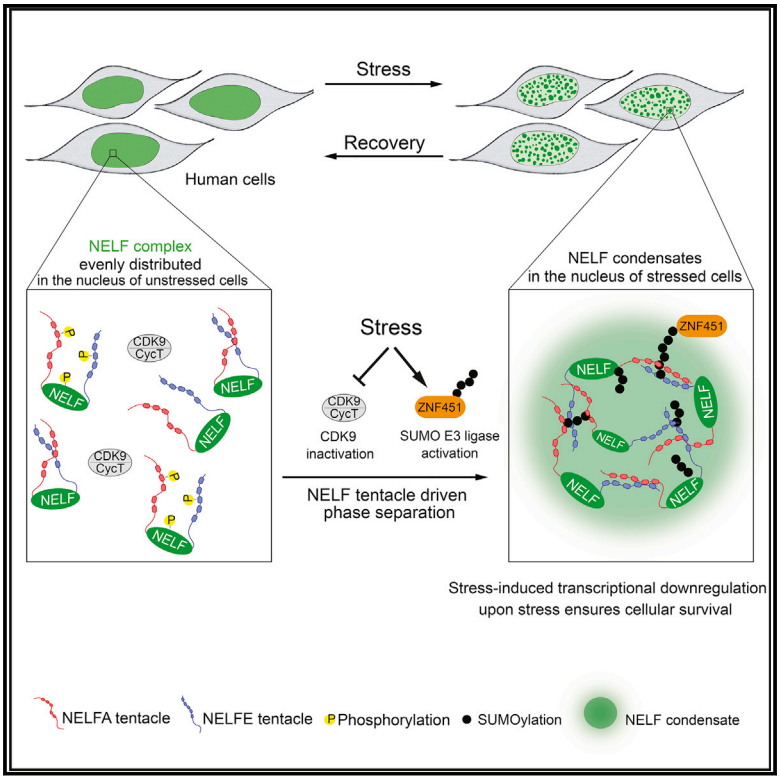

Highlights

- Transcription regulator NELF undergoes stress-induced condensation in human cells
- NELF condensation is regulated by its phosphorylation and SUMOylation
- Intrinsically disordered region of NELFA is necessary to drive condensation
- NELF condensation downregulates transcription to promote cell survival upon stress

Authors

Prashant Rawat, Marc Boehning, Barbara Hummel, ..., Andrea Pichler, Patrick Cramer, Ritwick Sawarkar

Correspondence

rawat@ie-freiburg.mpg.de (P.R.), patrick.cramer@mpibpc.mpg.de (P.C.), rs2099@cam.ac.uk (R.S.)

In Brief

Rawat et al. discovered stress-induced condensation of the transcriptional regulator NELF in human cells, recapitulated by phase separation of recombinant NELF *in vitro*. NELF condensation is governed by its disordered tentacles and stress-contingent changes in NELF phosphorylation and SUMOylation. NELF condensation facilitates stress-mediated transcriptional downregulation, supporting cell survival upon stress.

Rawat et al., 2021, Molecular Cell *81*, 1013–1026
March 4, 2021
https://doi.org/10.1016/j.molcel.2021.01.016

CellPress

Molecular Cell

CellPress
OPEN ACCESS

Article

Stress-induced nuclear condensation of NELF drives transcriptional downregulation

Prashant Rawat,[1,2,3,12,*] Marc Boehning,[4,12] Barbara Hummel,[1] Fernando Aprile-Garcia,[1] Anwit S. Pandit,[1,5,6] Nathalie Eisenhardt,[7] Ashkan Khavaran,[1,8] Einari Niskanen,[9] Seychelle M. Vos,[4,11] Jorma J. Palvimo,[9] Andrea Pichler,[7] Patrick Cramer,[4,*] and Ritwick Sawarkar[1,5,10,13,*]

[1]Max Planck Institute of Immunobiology and Epigenetics, Freiburg, Germany
[2]Faculty of Biology, University of Freiburg, Freiburg, Germany
[3]International Max Planck Research School for Molecular and Cellular Biology (IMPRS-MCB), Freiburg, Germany
[4]Department of Molecular Biology, Max Planck Institute for Biophysical Chemistry, Göttingen, Germany
[5]CIBSS, Centre for Integrative Biological Signaling Studies, Freiburg, Germany
[6]Spemann Graduate School of Biology and Medicine, Albert Ludwigs University of Freiburg, Freiburg, Germany
[7]Department of Epigenetics, Max Planck Institute of Immunobiology and Epigenetics, Freiburg, Germany
[8]Faculty of Medicine, University of Freiburg, Freiburg, Germany
[9]Institute of Biomedicine, University of Eastern Finland, Kuopio, Finland
[10]MRC, University of Cambridge, Cambridge, UK
[11]Present address: Department of Biology, Massachusetts Institute of Technology, Cambridge, MA, USA
[12]Equal Contribution
[13]Lead Contact
*Correspondence: rawat@ie-freiburg.mpg.de (P.R.), patrick.cramer@mpibpc.mpg.de (P.C.), rs2099@cam.ac.uk (R.S.)
https://doi.org/10.1016/j.molcel.2021.01.016

SUMMARY

In response to stress, human cells coordinately downregulate transcription and translation of housekeeping genes. To downregulate transcription, the negative elongation factor (NELF) is recruited to gene promoters impairing RNA polymerase II elongation. Here we report that NELF rapidly forms nuclear condensates upon stress in human cells. Condensate formation requires NELF dephosphorylation and SUMOylation induced by stress. The intrinsically disordered region (IDR) in NELFA is necessary for nuclear NELF condensation and can be functionally replaced by the IDR of FUS or EWSR1 protein. We find that biomolecular condensation facilitates enhanced recruitment of NELF to promoters upon stress to drive transcriptional downregulation. Importantly, NELF condensation is required for cellular viability under stressful conditions. We propose that stress-induced NELF condensates reported here are nuclear counterparts of cytosolic stress granules. These two stress-inducible condensates may drive the coordinated downregulation of transcription and translation, likely forming a critical node of the stress survival strategy.

INTRODUCTION

Environmental stress triggers a coordinated response in human cells to adapt them to altered conditions. Stress such as heat shock and arsenic exposure causes a rapid arrest of ongoing translation of mRNAs encoding metabolic, cell-cycle, and housekeeping proteins (Gibson, 2008; Holcik and Sonenberg, 2005). This is known to involve the formation of cytosolic stress granules—biomolecular condensates that form by liquid-liquid phase separation (LLPS) (Molliex et al., 2015). Cytosolic stress granules store inactivated ribosomes and mRNA, facilitating the rapid translational arrest caused by stress. Early studies showed that stressed cells also downregulate the transcription of most genes (Spradling et al., 1975). Recent genome-wide techniques confirmed that heat shock causes global transcriptional downregulation of housekeeping genes in fly, mouse, and human cells (Aprile-Garcia et al., 2019; Gressel et al., 2019; Mahat et al., 2016; Vihervaara et al., 2017). Transcriptional downregulation occurs at the level of promoter-proximal pausing of RNA polymerase (Pol) II, implicating the negative elongation factor (NELF) complex (Aprile-Garcia et al., 2019; Gressel et al., 2019), which is a hetero-tetramer composed of the subunits NELFA, B, C/D, and E.

Under normal conditions, Pol II transcribes 20–60 bases downstream of the transcription start site (TSS) and pauses for varying periods of time (Adelman and Lis, 2012; Core and Adelman, 2019; Core et al., 2008). The fate of promoter-proximally paused Pol II is determined by the opposing actions of negative and positive transcription elongation factors (Jonkers and Lis, 2015; Kwak and Lis, 2013). Recent structural studies of a paused Pol II complex have shown that NELF and 5,6-Dichloro-1-beta-D-ribofuranosylbenzimidazole (DRB)-sensitivity inducing factor

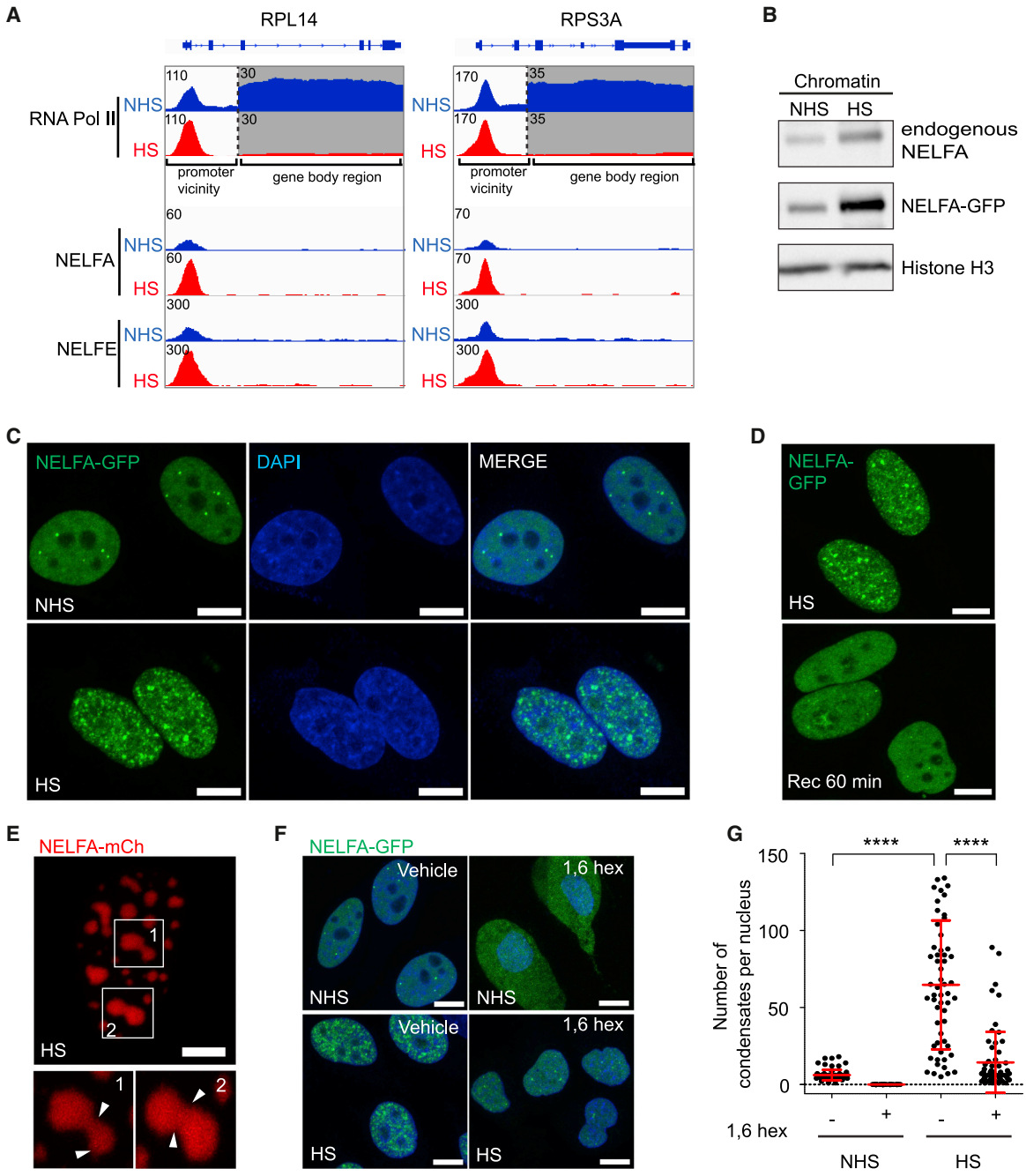

Figure 1. Stress induces NELF condensates in nuclei

(A) Genome browser tracks showing ChIP-seq occupancy of RNA Pol II, NELFA, and NELFE at RPL14 and RPS3A loci in HEK293 cells. Vertical scale indicates normalized read density in RPM. Top, RNA Pol II occupancy in gene body regions shown at a scale different than for promoter region. NHS, no heat shock; HS, heat shock (43°C). The gene models are shown with exons as boxes.

(B) Western blot analysis of indicated proteins after chromatin fractionation from HeLa cells exposed to heat shock (HS) compared to non-heat-shocked cells (NHS). Histone H3 was used for normalization.

(C) Fluorescence microscopy images of HeLa cells showing NELFA-GFP, DAPI, and merged signals. NHS, no heat shock; HS, heat shock. Scale bar indicates 10 μm.

(D) Fluorescence microscopy images of HeLa cells exposed to heat shock (HS) or recovered for 60 min following HS (Rec) showing NELFA-GFP signal. Scale bar indicates 10 μm.

(E) Fluorescence microscopy images of HeLa cells expressing NELFA-mCherry fusion protein exposed to HS. Inset images are magnified versions of demarcated white squares. White arrowheads in the magnified images mark presumed droplet fusion events. Scale bar indicates 10 μm.

(legend continued on next page)

(DSIF) bind to the polymerase in a manner that restricts Pol II mobility and impairs further RNA elongation (Vos et al., 2018b).

Release of Pol II from the paused state is facilitated by positive transcription elongation factor b (P-TEFb), which is composed of cyclin-dependent kinase 9 (CDK9) and cyclin T1 (CCNT1) (Marshall and Price, 1995; Price, 2000; Wei et al., 1998). CDK9 phosphorylates NELF and other factors to promote displacement of NELF from paused Pol II, concomitant with activation of Pol II and phosphorylation at Serine 2 on the pol II C-terminal domain (Kwak and Lis, 2013; Narita et al., 2003; Vos et al., 2018a; Wada et al., 1998; Yamaguchi et al., 1999). Under stress conditions, NELF binding to promoters of housekeeping genes is rapidly enhanced, coincident with a decrease of elongating Pol II (Aprile-Garcia et al., 2019). How stress leads to an increased residence time of NELF at downregulated gene promoters is not understood.

Recent studies have highlighted the importance of biomolecular condensation for the formation of membraneless organelles and cellular organization (Banani et al., 2017; Hyman et al., 2014; Shin and Brangwynne, 2017). Such condensation also occurs in the nucleus and was proposed to underlie transcriptional regulation (Hnisz et al., 2017). Indeed, recruitment of Pol II to promoters coincides with formation of "promoter condensates" containing transcription factors, transcriptional coactivators such as the Mediator complex, and Pol II (Boehning et al., 2018; Boija et al., 2018; Cho et al., 2018; Sabari et al., 2018). Elongating Pol II has recently been proposed to form "gene-body condensates" composed of elongation and RNA-processing factors (Cramer, 2019), and evidence for these condensates is accumulating (Guo et al., 2019; Lu et al., 2018). Nuclear condensates are likely formed by LLPS of proteins that possess intrinsically disordered regions (IDRs) (Alberti et al., 2019). Post-translational modification such as phosphorylation can influence the ability of IDR-containing proteins to facilitate condensation *in vivo* (Boehning et al., 2018; Guo et al., 2019; Lu et al., 2018).

Whereas transcription initiation and elongation of Pol II appear to be organized with the help of dedicated nuclear condensates, the intermediate state of paused Pol II is transient under normal conditions and, so far, has not been associated with biomolecular condensation. In this study, we uncover that stress triggers the formation of NELF condensates in the nucleus that are causally linked with decreased Pol II elongation and transcriptional downregulation. We propose that stress-induced NELF-based condensates are nuclear counterparts of cytosolic stress granules involved in downregulating gene expression.

RESULTS

Human NELF forms nuclear condensates upon stress

Heat shock stress causes global transcriptional downregulation, as seen by a decrease in the ChIP signal of RNA Pol II in gene bodies of many genes in human cells (Aprile-Garcia et al., 2019). We observed an increased binding of NELF at promoters of downregulated genes (Figure 1A). Consistent with this, biochemical fractionation further showed that heat shock caused an increase in the abundance of chromatin-associated NELF complex (Figures 1B and S1A). Strikingly, microscopic visualization of fluorescently tagged NELFA subunit revealed that the homogeneous nuclear signal re-organizes into bright nuclear puncta within 30 min of heat shock (Figure 1C). Stress-induced nuclear puncta were observed when the NELFA subunit was tagged with green fluorescent protein (GFP) or mCherry in live or in fixed cells (Figures 1C and S1B–S1E). In contrast, GFP alone remained homogenously distributed in heat-shocked cells (Figure S1F). Puncta formation of NELFA was observed even when cells were exposed to mild heat shock (Figure S1G) or arsenic stress (Figure S1H). Subunits NELFC/D and NELFE also formed puncta upon heat shock that overlapped with NELFA puncta (Figures S2A–S2C), suggesting that the entire NELF complex is reorganized into nuclear puncta upon various cellular stresses. Importantly, similar stress-induced puncta were observed for chromatin-associated endogenous NELFA using immunofluorescence imaging (Figures S2D and S2E). Fluorescence-activated cell sorting (FACS) analyses after pre-extracting non-chromatin-bound proteins further confirmed that stress enhanced chromatin retention of endogenous NELF (Figure S2F). Stress-induced NELF puncta reverted to homogeneous signal within 30 min of recovery from stress (Figures 1D and S2G), arguing against an irreversible aggregation of NELF upon stressful conditions. The NELF puncta showed liquid-like properties such as spherical shape (Figures S2H and S2I) and rapidly coalesced to form bigger spherical puncta (Figure 1E). To further test if NELF puncta were condensates formed by LLPS, we treated cells with 1,6-hexanediol—an aliphatic alcohol that is thought to disrupt weak hydrophobic interactions that underlie many phase-separated condensates (Kroschwald et al., 2017). NELF puncta were highly sensitive to 1,6-hexanediol treatment as quantified by the number of cells with NELF puncta (Figures 1F and S2J) and the number of condensates per nucleus (Figures 1F and 1G). Thus, human NELF complex rapidly formed liquid-like condensates upon stress, concomitant with increased recruitment of NELF to chromatin and global transcriptional downregulation.

Recombinant NELF undergoes phase separation *in vitro*

Given the ability of human NELF to form condensates in cells, we wanted to test whether NELF was capable of undergoing LLPS *in vitro*. We expressed recombinant human NELF complex in insect cells, purified and dephosphorylated it, and labeled it with a fluorescent dye (Figure S3A). Confocal fluorescence microscopy showed that purified NELF readily self-associated to form numerous, micron-sized spherical droplets, which settled onto

(F) Fluorescence microscopy images of HeLa cells expressing NELFA-GFP and treated with vehicle or 1,6 hexanediol (1,6 hex). NHS, no heat shock; HS, heat shock. Scale bar indicates 10 μm.

(G) Graph showing the number of NELFA-GFP condensates per nucleus in HeLa cells exposed to indicated conditions. NHS, no heat shock; HS, heat shock; 1,6 hex, 1,6 hexanediol. Each dot represents data for one nucleus. Asterisks denote p value of <0.0001 as calculated by the one-way ANOVA with Dunnet's multiple comparison tests.

See also Figures S1 and S2.

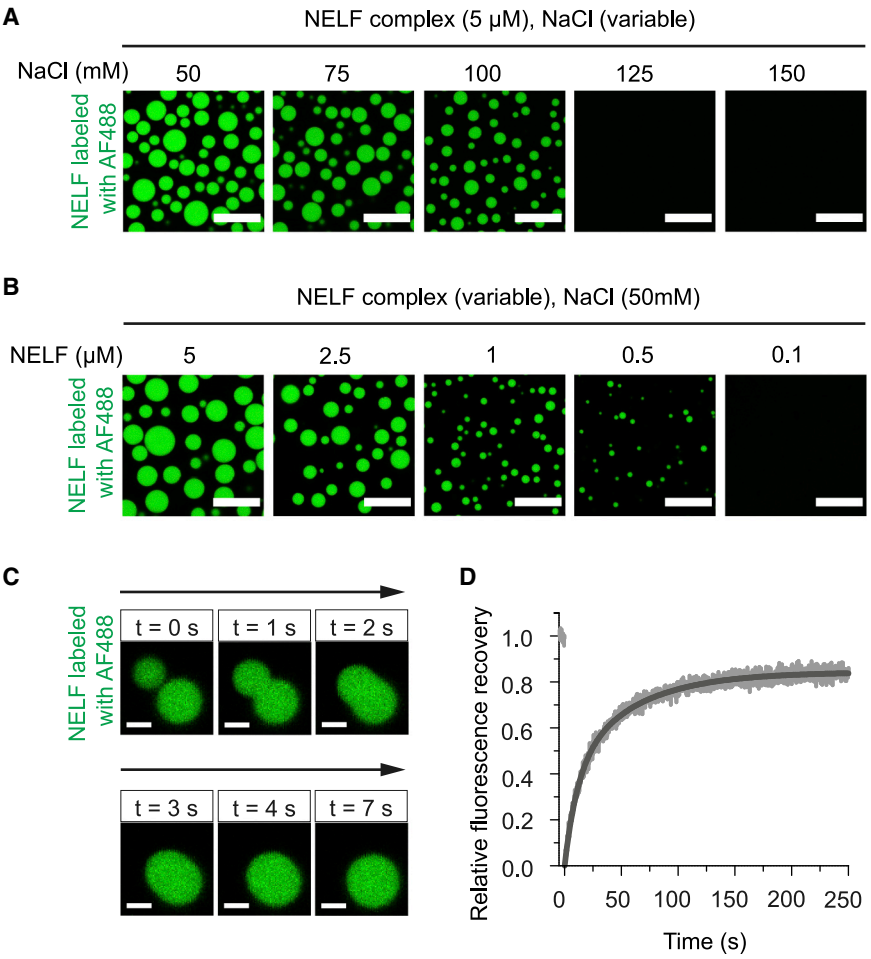

Figure 2. NELF complex undergoes liquid-liquid phase separation *in vitro*

(A) Fluorescence microscopy images of purified recombinant NELF complex in buffer with variable NaCl concentration, as indicated. AF488, Alexa Fluor 488. Scale bar denotes 20 μm.

(B) Fluorescence microscopy images of purified recombinant NELF complex at variable protein concentrations, as indicated. Scale bar denotes 20 μm.

(C) Time series showing fusion of NELF droplets *in vitro*. t indicates time in seconds. Scale bar indicates 2 μm.

(D) Relative quantification of fluorescence recovery kinetics of NELF droplets following partial droplet bleaching. The FRAP curve shows the mean and standard error (light gray) across three independent replicates and was fit to a double-exponential recovery curve (dark gray line).

See also Figure S3.

the coverslip surface by gravity (Figure 2A). These observations indicated that NELF is capable of undergoing phase separation *in vitro* in the absence of crowding agents.

NELF droplet formation was sensitive to increasing ionic strength (Figure 2A), suggesting that electrostatic interactions were required for NELF LLPS *in vitro*. At a concentration of sodium chloride of 50 mM, NELF formed droplets with a critical concentration of ~0.5 μM (Figure 2B). Upon contact, these droplets coalesced into larger ones that readily relaxed to a spherical shape (Figure 2C), emphasizing the liquid-like properties of NELF droplets. To study the dynamics of molecules within NELF phase-separated droplets, we used fluorescence recovery after photobleaching (FRAP). Rapid recovery of fluorescence within the bleached region (Figures 2D and S3B) showed that NELF molecules can freely diffuse within the condensed phase, consistent with their liquid-like behavior. Together, these results demonstrate that the purified NELF complex can undergo LLPS *in vitro*.

NELF dephosphorylation is required for condensation

We next investigated why NELF condensation was observed only upon stress. We speculated that stress induces changes in post-translational modifications of NELF that may be critical for condensation. Mass spectrometric analysis of NELF isolated from control and heat-shocked human cells indeed revealed robust changes in phosphorylation of NELF subunits upon heat shock. A consistent decrease in phosphorylation levels of three NELFA residues was observed upon heat shock (Figure 3A). It is known that these NELF residues are phosphorylated by the P-TEFb kinase subunit CDK9 *in vivo* (Lu et al., 2016).

To study the role of P-TEFb-mediated phosphorylation in NELF condensation, we incubated preformed NELF droplets with active wild-type (WT) or catalytically inactive P-TEFb complex *in vitro*. Time-resolved imaging revealed that NELF droplets shrunk considerably when treated with active P-TEFb, whereas no effect was observed with the inactive P-TEFb variant (Figure 3B). We confirmed that P-TEFb phosphorylated the NELF complex under *in vitro* conditions (Figures S3C and S3D). To further test the effect of phosphorylation on NELF phase separation, we performed FRAP analyses on partial or entire droplets formed by dephosphorylated or P-TEFb-treated NELF (Figures 3C, 3D, and S3E). After photobleaching entire droplets, about 80% of phosphorylated NELF molecules exchanged with the surrounding solution within 20 min, while only 40% of dephosphorylated NELF molecules recovered in an equally sized droplet (Figures 3C and 3D). Consistently, P-TEFb-treated NELF showed faster fluorescence recovery after photobleaching a spot within individual droplets (Figure S3E). The faster recovery of P-TEFb-treated NELF indicates that phosphorylation weakens the intermolecular interactions between NELF molecules, in line with the observed correlation between NELF dephosphorylation and condensation (Figure 3B).

To investigate how stress could regulate the phosphorylation of NELF in cells, we performed a quantitative interactome analysis on the kinase subunit of P-TEFb, namely CDK9. The interaction between CDK9 and the HSP90 chaperone complex did not

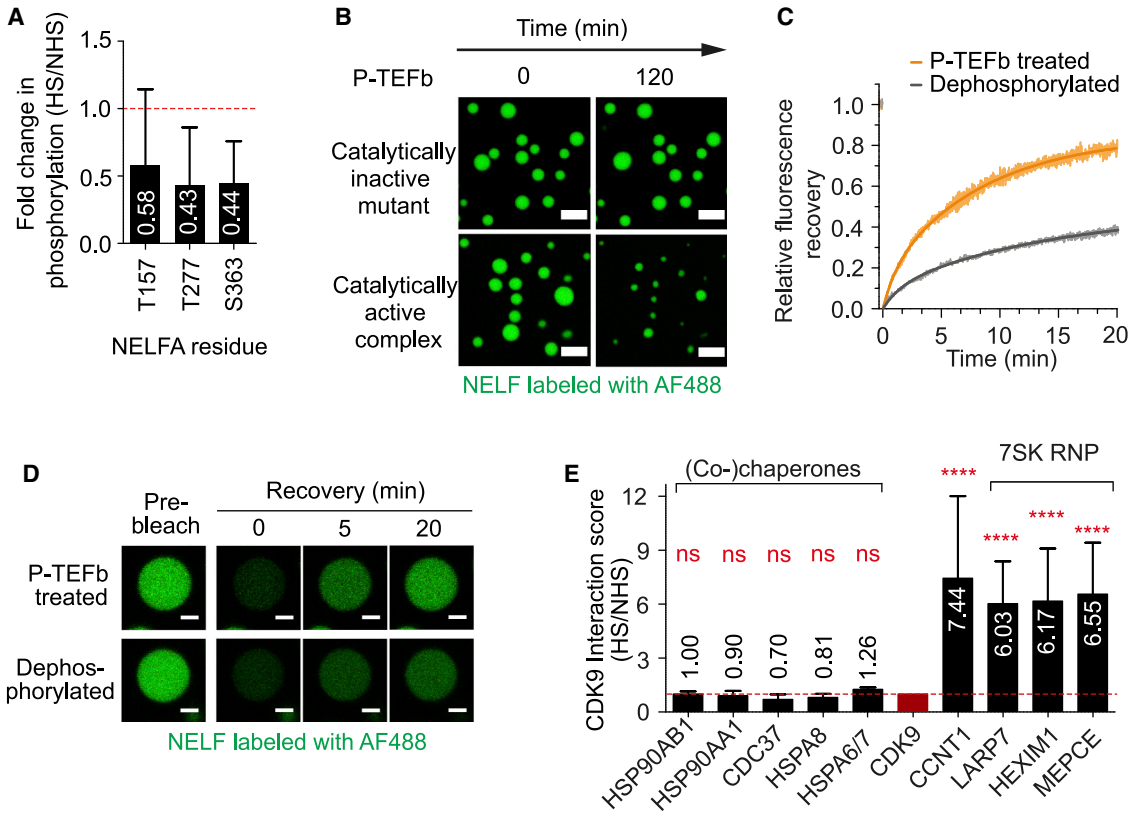

Figure 3. NELF dephosphorylation is required for phase separation

(A) Mean fold changes in phosphorylation levels of indicated NELFA residues in HEK293 cells in heat-shocked cells (HS) compared to non-heat-shocked cells (NHS), as detected by mass spectrometry. Error bars represent SD (n = 3 independent cell cultures). Red dotted line denotes the mean phosphorylation level in non-heat-shocked cells.

(B) Fluorescence microscopy images of recombinant AF488-labeled NELF droplets that were incubated with P-TEFb containing either active WT CDK9 or a catalytically inactive CDK9 variant. NELF droplets were incubated with P-TEFb for 120 min. Scale bar indicates 5 μm.

(C) Relative fluorescence recovery kinetics of dephosphorylated (gray) or P-TEFb-treated (orange) NELF following full droplet bleaching. The curve shows the mean and standard error (light gray or orange) across three experiments and was fit to a double-exponential recovery curve (dark gray or orange).

(D) Representative fluorescence microscopy images of the full droplet bleaching experiment shown in (C). Scale bar indicates 2 μm.

(E) Heat-shock-induced changes in CDK9-interaction scores of indicated proteins quantified by mass spectrometry in HEK293 cells. A value of 1 denoted by a dotted red line indicates no change in interaction with CDK9 upon heat shock. Error bars represent SD (n = 3 independent cell cultures). Asterisks denote p value of <0.0001 as calculated by one-way ANOVA with Dunnett's multiple comparison tests. ns denotes non-significant.

See also Figure S3.

change during heat shock (Figures 3E and S3F). However, heat shock caused a significant increase in the interaction of CDK9 with LARP7, HEXIM1, and MEPCE (Figure 3E). These proteins are known components of the 7SK ribonucleoprotein (RNP) complex that sequesters CDK9 in a functionally inactive form (Nguyen et al., 2001; Yang et al., 2001). To test the hypothesis that CDK9 sequestration upon heat shock leads to NELF condensation, we overexpressed CDK9 and its cyclin partner CCNT1 that together form the P-TEFb complex. A significant reduction in number of cells showing NELFA condensates was observed in cells overexpressing P-TEFb (Figure S3G). Moreover, survival after heat shock was significantly compromised in cells overexpressing P-TEFb or just CCNT1 (Figure S3H). Taken together, these results suggest that heat shock leads to CDK9 sequestration, likely promoting NELF dephosphorylation and condensation.

Stress-induced SUMOylation is required for NELF condensation

CDK9 inhibition with DRB on its own did not lead to NELF condensate formation (Figures 4A and S3I), implying that a decrease in NELF phosphorylation alone was not sufficient to drive cellular NELF condensation. In addition, we found that heat shock causes conjugation of Small Ubiquitin-like Modifier (SUMO) 2/3 at more than 30 residues of the NELF complex (Hendriks et al., 2018; Hendriks et al., 2017) (Figure S4A), suggesting a role of SUMOylation in NELF condensation. We observed that protein SUMOylation and NELF condensation is initiated within 5 min of acute heat shock (Figures S4B and S4C), whereas transcriptional downregulation is robustly observed after 15 min of exposure to heat shock (Aprile-Garcia et al., 2019). Treatment of cells with ML-792, an inhibitor of SUMO Activating Enzyme 1/2 (SAE1/2), blocked the stress-induced increase of SUMOylation

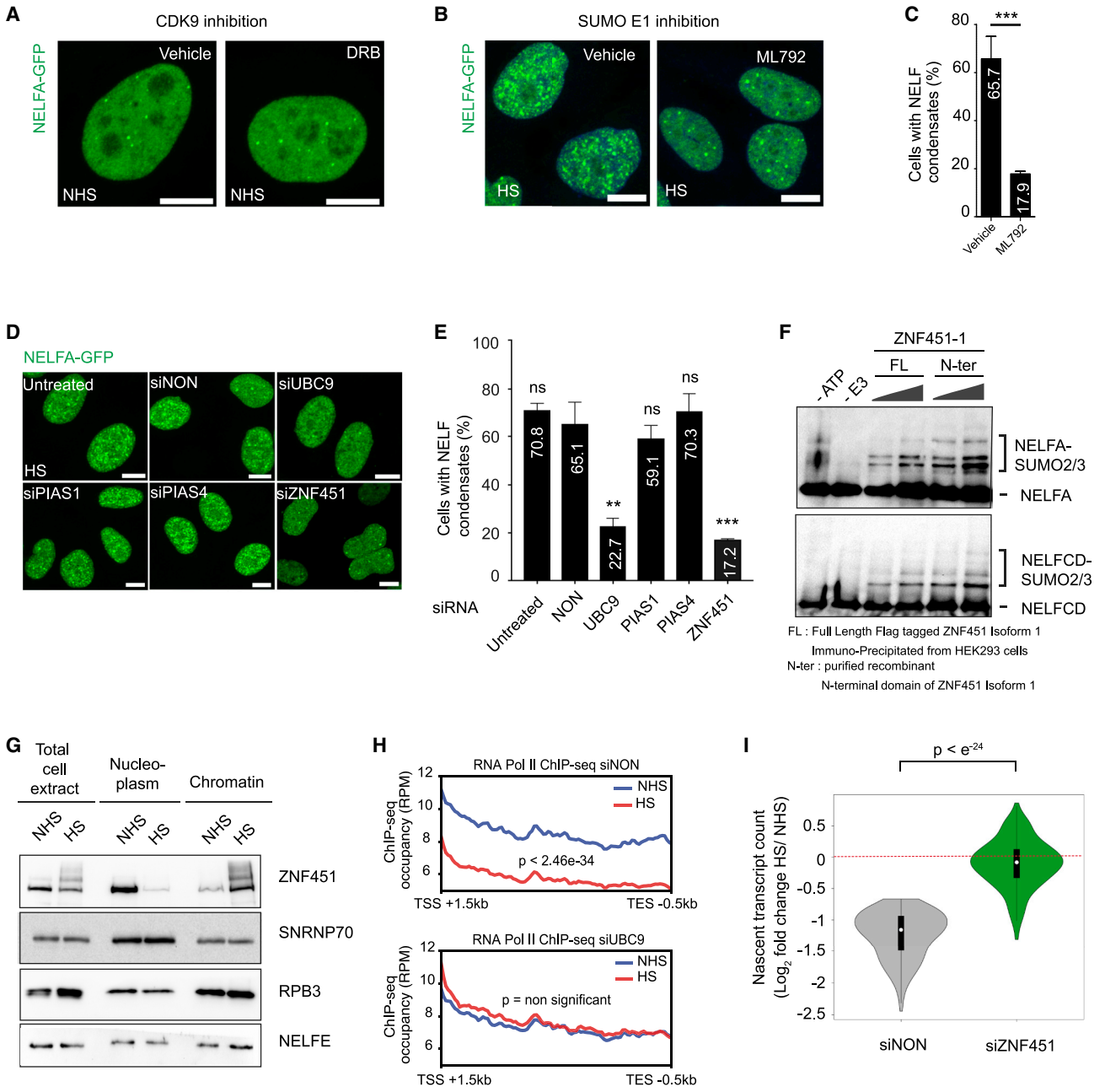

Figure 4. NELF SUMOylation drives nuclear condensate formation

(A) Fluorescence microscopy images of HeLa NELFA-GFP cells treated with vehicle or CDK9 inhibitor 5,6-Dichloro-1-β-d-ribofuranosylbenzimidazole (DRB) under no heat shock conditions (NHS). Scale bar indicates 10 μm.

(B) Fluorescence microscopy images of HeLa NELFA-GFP cells exposed to heat shock (HS) and treated with vehicle or ML-792. Scale bar indicates 10 μm.

(C) Percentage of cells with NELFA condensates after heat shock in vehicle or ML-792 treated samples. Data quantification of (B). Error bars represent SD ($n = 2$ independent cell cultures). Asterisks denote p value <0.001 as calculated by two-tailed unpaired t test.

(D) Fluorescence microscopy images of heat-shocked HeLa cells expressing NELFA-GFP. Cells were treated with siRNAs against SUMO E2 conjugating enzyme (UBC9), SUMO E3 ligases (PIAS1, PIAS4, and ZNF451), non-targeting siRNA (siNON), or left untreated. Scale bar indicates 10 μm.

(E) Percentage of heat-shocked HeLa cells with NELFA condensates from experiment described in (D). Error bars represent SD ($n = 2$ independent replicates). Conditions compared to siNON. Asterisks denote p value of (***, 0.001; **, 0.01) as calculated by one-way ANOVA with Dunnett's multiple comparison tests.

(F) Western blot analyses of NELF after performing *in vitro* SUMOylation reactions using NELFA (top) and NELFC/D antibodies (bottom). Either immunoprecipitated full-length E3 ligase ZNF451 or a recombinant N-terminal fragment were used at two different concentrations (STAR Methods). Reactions lacking ATP or ZNF451 serve as negative controls.

(legend continued on next page)

(Figure S4D) and reduced the number of NELF condensates (Figures 4B, 4C, and S4E). Small interfering RNA (siRNA)-mediated knockdown of SUMO-conjugating E2 enzyme UBC9 also decreased the fraction of cells with NELF condensates (Figures 4D, 4E, and S4F). Together, these data strongly support the idea that heat-shock-induced SUMOylation is critical for NELF condensation.

A focused siRNA screen for SUMO E3 ligases led us to observe that ZNF451 depletion reduced NELF condensation to an extent similar to UBC9 depletion (Figures 4D, 4E, and S4F), suggesting that ZNF451 SUMOylates NELF in stressed cells. Indeed, ZNF451 isoform 1 immunoprecipitated from human cells (Eisenhardt et al., 2015) as well as an N-terminal region of ZNF451 isoform 1 purified from *E. coli* could SUMOylate recombinant NELF *in vitro* (Figures 4F and S4G). Coincidently, ZNF451 was the only SUMO E3 ligase whose abundance at chromatin was drastically increased in response to heat shock, similar to the NELF complex (Figures 4G and S4H). Reminiscent of the auto-SUMOylated forms of ZNF451 seen *in vitro* (Figure S4G), we also observed high molecular weight forms in heat-shocked cells (Figure 4G). Overexpression of ZNF451 led to an increased fraction of cells showing larger NELF condensates (Figures S5A and S5B), supporting the view that ZNF451-mediated SUMOylation facilitates NELF condensation. Intriguingly, ZNF451 itself formed puncta that were located at the periphery of NELF condensates (Figure S5B). ZNF451 overexpression significantly reduced cell viability upon heat shock, similar to P-TEFb overexpression (Figure S5C). Strikingly, however, the overexpression of both ZNF451 and P-TEFb neutralized the individual effects on cellular survival upon heat shock (Figure S5C). These observations buttress the possibility that the two independent pathways, ZNF451-mediated SUMOylation and P-TEFb-mediated phosphorylation, have antagonizing functions in the process of NELF condensation.

We then tested the significance of SUMOylation in stress-mediated transcriptional downregulation by pol II chromatin immunoprecipitation sequencing (ChIP-seq) (Mahat et al., 2016; Niskanen et al., 2015) and nascent transcript counting with SLAM-seq (Herzog et al., 2017). UBC9 depletion by siRNA blocked stress-induced downregulation of hundreds of genes as assessed by Pol II ChIP-seq (Figures 4H, S5D, and S5E). Similarly, ZNF451-depleted cells showed impaired downregulation of genes upon stress recovery as shown by Thiol(SH)-linked alkylation for the metabolic sequencing of RNA (SLAM-seq) (Figures 4I and S5F). These results indicate that stress-induced SUMOylation mediated by UBC9/ZNF451 is necessary for global transcriptional downregulation seen upon stress. Besides ZNF451, pro-myelocytic leukemia (PML) is another protein which has been associated with nuclear SUMOylation (Sahin et al., 2014) and a known target of ZNF451 (Eisenhardt et al., 2015). We ruled out the functional involvement of PML in NELF condensation, as PML-depleted cells formed NELF puncta similar to WT cells upon heat shock (Figure S5G). Thus, heat shock activates the UBC9/ZNF451 pathway leading to NELF SUMOylation, NELF condensation, and transcriptional downregulation.

NELF condensates are distinct from HSF1-containing nuclear stress bodies

Upon stress, mammalian cells are known to form stress-induced nuclear bodies marked by the presence of the heat shock factor 1 (HSF1) (Biamonti and Vourc'h, 2010; Cotto et al., 1997). While both NELF and HSF1 are homogenously distributed in the nucleus in non-stressed cells, we found that NELF and HSF1 formed spatially distinct puncta upon heat shock without any overlap (Figure S6A). This observation suggests that NELF condensates are structurally and likely functionally distinct from nuclear stress bodies.

HSF1 is critical for upregulation of chaperone-encoding genes during heat shock but dispensable for global downregulation (Aprile-Garcia et al., 2019; Mahat et al., 2016). As expected, heat shock caused an increase in the Pol II ChIP-seq occupancy at promoters of heat shock-induced genes (Figure S6B). Concomitantly, NELF occupancy also increased at these promoters to a similar extent (Figure S6B), in line with the known function of NELF as a Pol II co-factor. At promoters of downregulated genes, however, NELF ChIP-seq signal increased without any change of Pol II occupancy (Figure S6B). Thus, heat shock causes significantly more NELF to accumulate in comparison with Pol II at downregulated genes (Figure S6C), and this NELF accumulation correlates strongly with transcriptional downregulation (Figure S6D).

NELF tentacles drive phase separation and interact with Pol II CTD *in vitro*

NELFA and NELFE both contain IDRs termed "tentacles" (Figures 5A and S6E–S6G) (Vos et al., 2018b). GFP fused to either NELFA or NELFE tentacles did not undergo phase separation (Figure 5B). However, when the GFP-NELFA tentacle fusion protein was mixed in an equimolar ratio with the GFP-NELFE tentacle fusion protein, droplets formed readily (Figure 5C). GFP that fused to NELFE tentacle at its N terminus and NELFA tentacle at its C terminus Figure S5 exhibited phase separation even at much lower concentrations (Figure 5D). The obtained droplets were sensitive to 1,6-hexanediol (Figure 5E). Importantly, the NELF complex variants lacking either the NELFA or NELFE

(G) Western blot analysis of ZNF451 and NELFE is shown for indicated fractions from HeLa cells exposed to heat shock (HS) or no heat shock (NHS). SNRNP70 and RPB3 are used as loading controls.
(H) Effect of SUMO E2 (UBC9) depletion on HS-induced changes in RNA Pol II ChIP-seq occupancy in gene body regions of top 250 expressed genes. Regions from transcription start site (TSS) +1.5 kb to transcription end site (TES) –0.5 kb are shown. p value from Wilcoxon test is indicated (n = 2 independent cell cultures).
(I) Effect of SUMO E3 ligase ZNF451 depletion on HS-induced changes in nascent transcript counts as quantified by SLAM-seq in HeLa cells. Significantly downregulated genes in siNON cells as calculated by differential gene expression analysis based on the negative binomial distribution (DESeq2) are used. The red line indicates no change in expression. The violin plot depicts median, interquartile range, and 95% confidence interval with white dot, black bar, and thin black line, respectively. p value from Wilcoxon test is indicated (n = 3 independent cell cultures).
See also Figures S3–S5.

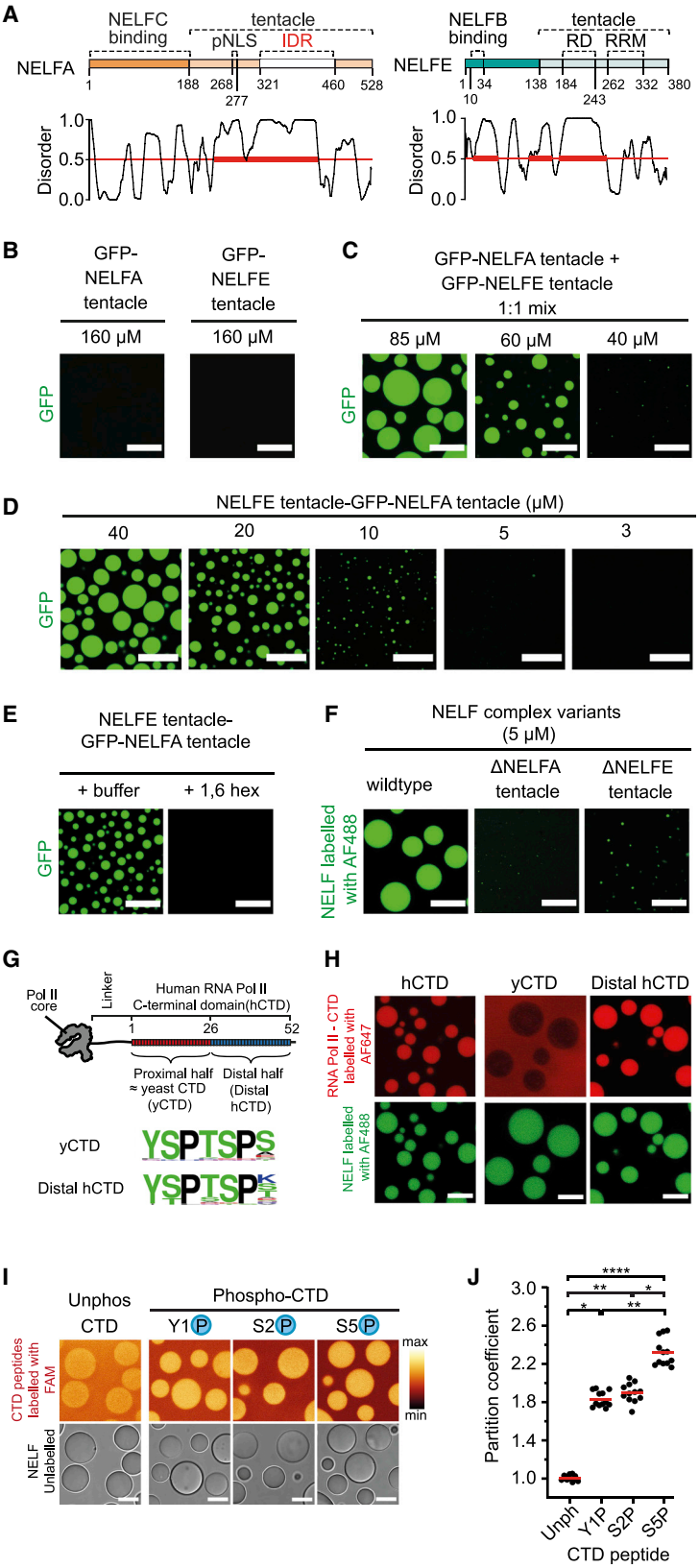

Figure 5. NELF tentacles drive phase separation *in vitro*

(A) Domain architecture of NELFA and NELFE subunits with corresponding disorder prediction using the software PONDR (Peng et al., 2006). pNLS, putative nuclear localization sequence; IDR, intrinsically disordered region; RD, Arg/Asp-rich domain; RRM, RNA recognition motif.

(B) Phase separation assays with recombinant GFP-NELFA or GFP-NELFE tentacle fusion protein at low ionic strength (50 mM NaCl). Scale bar corresponds to 20 μm.

(C) Phase separation assays with equimolar mixtures of recombinant GFP protein fused to either the NELFA or NELFE tentacle region at 50 mM NaCl. The concentration at which each protein was used is indicated. Scale bar corresponds to 20 μm.

(D) Fluorescence microscopy images of concentration-dependent LLPS of purified recombinant double tentacle GFP fusion protein, which contains the NELFA and the NELFE tentacles at C and N terminus, respectively. Scale bar indicates 20 μm.

(E) Phase separation assays with the double tentacle GFP protein containing NELFA and NELFE tentacles in the presence or absence of 10% 1,6 hexanediol (1,6 hex). Scale bar indicates 20 μm.

(F) Phase separation assays with recombinant purified NELF complex that lacks either the NELFA tentacle (ΔNELFA tentacle) or the NELFE tentacle (ΔNELFE tentacle). Scale bar indicates 20 μm.

(G) Scheme of the human RNA Pol II C-terminal domain (hCTD) with its 52 heptad repeats, which is composed of a yeast CTD-like proximal half (1–26 repeats) and a distal half (27–52 repeats). Sequence motifs of the CTD constructs used in the partitioning assays are shown below (Portz et al., 2017).

(H) Partitioning of different CTD constructs relative to the NELF droplet phase visualized by fluorescence microscopy. Scale bars correspond to 10 μm.

(I) Partitioning of carboxyfluorescein (FAM)-labeled CTD peptides relative to unlabeled NELF droplets visualized by fluorescence and brightfield microscopy. CTD peptides were either unphosphorylated (Unphos CTD) or phosphorylated at tyrosine-1 (Y1P), serine-2 (S2P), or serine-5 (S5P). For better visualization, the fluorescence images are displayed using a multicolor representation (color map representing the minimum [min] and maximum [max] intensity is shown). Scale bars correspond to 10 μm.

(J) Quantification of partition coefficients of the different CTD peptides shown in (I). Individual dots (n = 12) represent coefficients calculated from different recorded images. Red lines correspond to the mean, and asterisks denote the p values as determined by the Kruskal-Wallis and Dunn's multiple comparison tests (*, $p < 0.05$; **, $p < 0.01$; ***, $p < 0.001$; ****, $p < 0.0001$).

See also Figure S6.

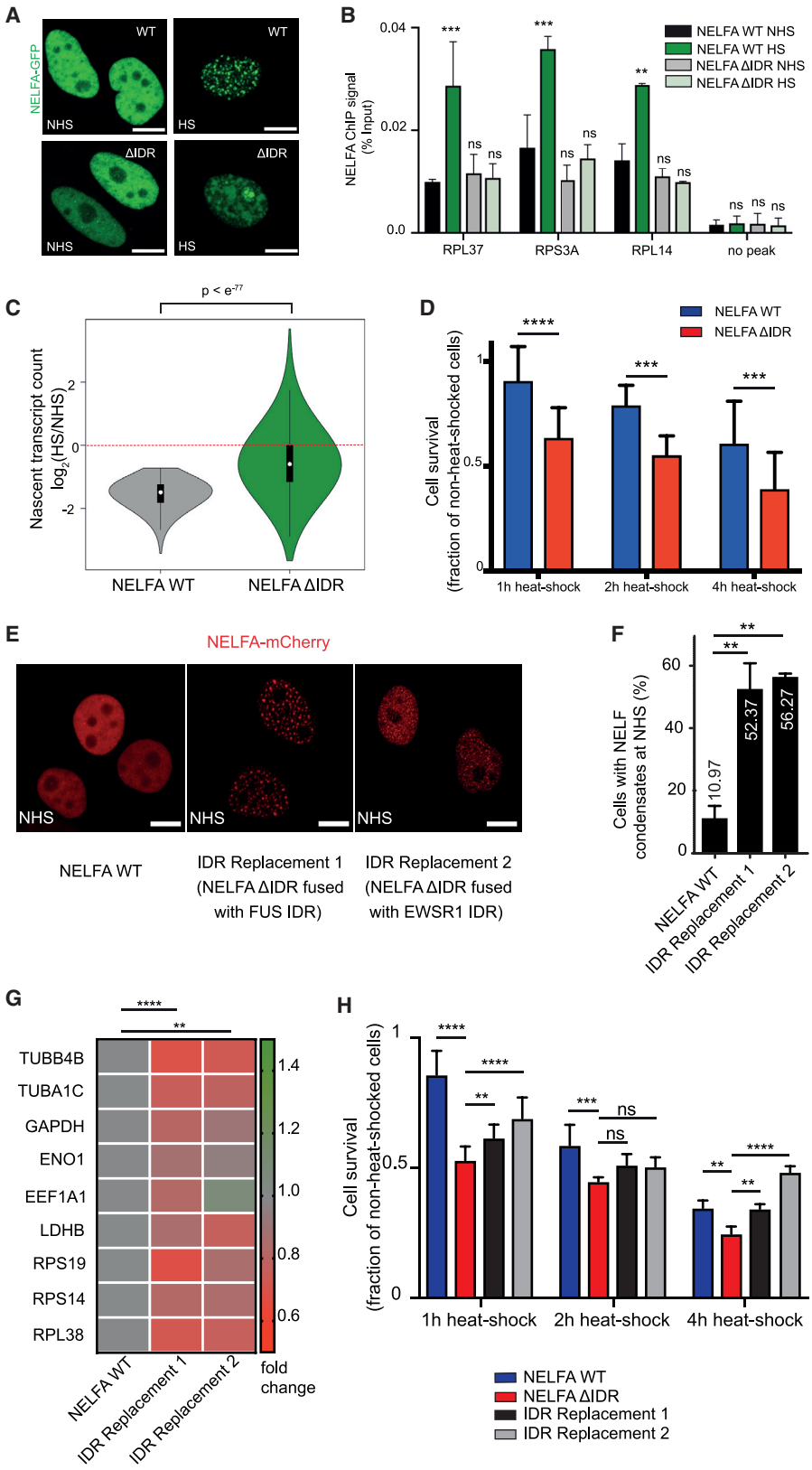

(legend on next page)

tentacle showed a highly reduced ability to form liquid droplets (Figures 5F and S6E). Taken together, our *in vitro* data identified the two disordered tentacles as critical determinants that are necessary and sufficient for LLPS of the NELF complex.

The disordered carboxy-terminal heptad-repeat domain (CTD) of Pol II can form homotypic and heterotypic interactions with IDRs of several transcription factors depending on its phosphorylation state (Boehning et al., 2018; Guo et al., 2019; Kwon et al., 2013). Enrichment of human CTD (hCTD) within NELF droplets (Figures 5G and 5H) suggests that NELF condensates can indeed form heterotypic interactions with CTD. The proximal half of hCTD contains mostly repeats with the consensus sequence $Y_1S_2P_3T_4S_5P_6S_7$ and is almost identical to the CTD of the yeast *S. cerevisiae* (yCTD) (Figure 5G). The distal half of hCTD consists of repeats that frequently deviate from the consensus, most commonly at heptad position 7 (Figure 5G) (Harlen and Churchman, 2017). Strikingly, the distal hCTD half showed enrichment within NELF droplets, but yCTD was excluded from NELF droplets (Figure 5H). These observations suggest an importance of the distal non-consensus repeats in the hCTD-NELF condensate interaction. Experiments investigating the partitioning of synthetic CTD peptides with distinct phosphorylated residues revealed that S_5-phosphorylated peptide was enriched within NELF droplets more than other tested CTD peptides (Figures 5I and 5J). The S_5-phosphorylated form of Pol II is primarily observed around the promoter-proximal region where NELF occupancy increases upon heat shock (Figure 1A) (Aprile-Garcia et al., 2019; Eick and Geyer, 2013; Harlen and Churchman, 2017).

A disordered NELFA region drives NELF condensation in cells, transcriptional downregulation, and survival upon stress

By deletion mutagenesis of the NELFA tentacle, we identified a continuous region of disorder from residue 321 to 460, which we refer to as the IDR. NELFA lacking the IDR (NELFA-ΔIDR) showed normal targeting to the nucleus, as a putative nuclear localization sequence (pNLS) identified in the tentacle (Figure S6H) was not inside the IDR (Figure 5A). NELFA-ΔIDR also got incorporated in the NELF complex (Figures S6I and S6J). However, NELFA-ΔIDR failed to form condensates upon heat shock, unlike its WT counterpart (NELFA-WT) (Figures 6A, S6K, and S6L), in agreement with the *in vitro* phase separation data (Figures 5F and S6E). Quantification by ChIP-qPCR showed that both NELFA-WT and NELFA-ΔIDR were recruited to target promoters to the same extent in unstressed cells. Heat shock caused an increase of NELFA-WT ChIP signal at promoters of downregulated genes (Figures 1A and 6B); however, this increase was not seen for NELFA-ΔIDR (Figure 6B). We and others have shown previously (Aprile-Garcia et al., 2019; Mahat et al., 2016) that hundreds of genes encoding growth-related biosynthetic proteins become transcriptionally downregulated upon heat shock in NELFA-WT cells (Figures S7A–S7E). However, cells expressing NELFA-ΔIDR were unable to downregulate these genes (Figures 6C and S7C–S7E). Instead, genes encoding growth-promoting cell cycle, translation, and DNA replication proteins were transcriptionally upregulated in NELFA-ΔIDR cells (Figures S7I and S7J). Heat-shock-mediated transcriptional upregulation of chaperone-encoding genes was similar in NELFA-WT and NELFA-ΔIDR cells (Figures S7A–S7H). Thus, deletion of the NELFA IDR and loss of NELF condensation specifically compromised NELF function in stress-induced transcriptional downregulation. NELFA-ΔIDR cells showed a marked decrease of cell survival upon heat shock compared to NELFA-WT cells (Figure 7D), suggesting that IDR-driven NELF condensation is adaptive for stress resistance.

To establish a causal relationship between NELF condensation and its stress-related function, we fused NELFA-ΔIDR to IDRs of unrelated proteins. These replacement constructs contained the IDR from either FUS or EWSR1, two proteins known to be phase separated even under non-heat-shock conditions

Figure 6. NELFA disordered region drives stress-induced nuclear NELF condensation, transcriptional downregulation, and cell survival upon stress

(A) Fluorescence microscopy images of HeLa cells expressing GFP fused to either wild-type NELFA (WT) or NELFA containing 140-residue IDR deletion (ΔIDR). NHS, no heat shock; HS, heat shock. Scale bar indicates 10 μm.

(B) ChIP-qPCR measuring NELFA occupancy at indicated gene promoters in HeLa cells stably expressing NELFA-GFP protein with either WT or ΔIDR NELFA. "No peak" primer set amplifies a genomic region not expected to bind NELFA and acts as a negative control. The y axis indicates the mean percent of immunoprecipitated DNA relative to starting input material. Error bars represent SD ($n = 2$, independent cell cultures). Asterisks denote p value (***, 0.001; **, 0.01) as calculated by two-way ANOVA with Sidak's multiple comparison tests. ns denotes non-significant.

(C) Effect of deletion of NELFA IDR on HS-induced changes in nascent transcript counts as quantified by SLAM-seq in HeLa cells. Significantly downregulated genes in NELFA-WT cells upon heat shock as calculated by DESeq2 are used. The red line indicates no change in expression. The violin plot depicts median, interquartile range, and 95% confidence interval with white dot, black bar, and thin black line, respectively. p value from Wilcoxon test is indicated.

(D) Normalized fraction of viable HeLa cells expressing NELFA-WT or -ΔIDR after exposure to heat shock (HS) for the indicated time and subsequent recovery for 24 h. Error bars represent SD ($n = 6$ independent cell cultures). Asterisks denote p value (****, 0.0001; ***, 0.001) as calculated by two-way ANOVA with Sidak's multiple comparison tests.

(E) Fluorescence microscopy images of HeLa cells expressing mCherry-tagged wild-type NELFA (WT) or NELFA-ΔIDR fused to FUS IDR (Replacement 1) or EWSR1 IDR (Replacement 2). NHS, no heat shock. Scale bar indicates 10 μm.

(F) Percentage of cells with NELFA condensates under no heat shock conditions (NHS). Quantification of the experiment described in (A). Error bars represent SD ($n = 2$ independent cell cultures). Asterisks denote p value of 0.01 as calculated by one-way ANOVA with Dunnett's multiple comparison tests.

(G) RT-qPCR-based nascent-transcript quantification in non-heat-shocked HeLa cells expressing NELFA-WT, IDR replacement 1, or IDR replacement 2. The mean transcript level calculated from n = 4 independent cell cultures is shown for the indicated genes. Asterisks denote p value (****, <0.0001; **, 0.01) as calculated by one-way ANOVA with Dunnett's multiple comparison tests.

(H) Normalized fraction of viable HeLa cells expressing NELFA-WT, IDR replacement 1, or IDR replacement 2 after exposure to heat shock (HS) for the indicated time and subsequent recovery for 24 h. Error bars represent SD ($n = 6$ independent cell cultures). Asterisks denote p value (****, <0.0001; ***, 0.001; **, 0.01) as calculated by two-way ANOVA with Sidak's multiple comparison tests. ns denotes non-significant.

See also Figures S6 and S7.

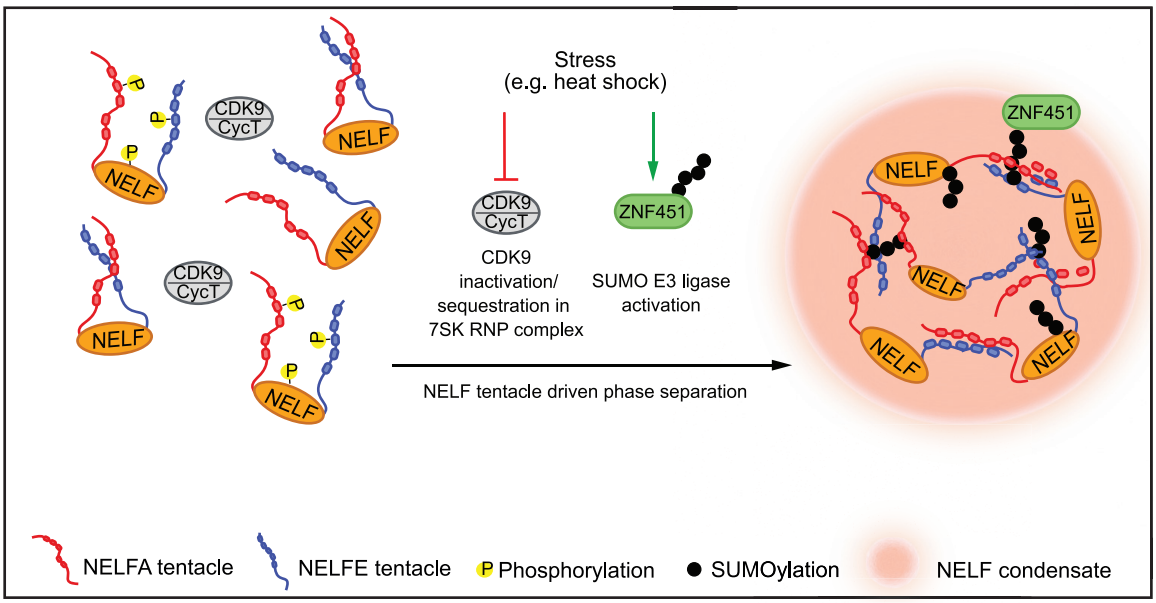

Figure 7. Model for the regulation of NELF condensation upon stress such as heat shock

The interaction between NELFA and NELFE tentacles of NELF complex are essential drivers of the NELF phase separation. The integration of two stress-dependent pathways—sequestration of P-TEFb complex and activation of SUMO E3 ligase ZNF451—results in NELF condensation in nuclei of stressed cells.

(Harrison and Shorter, 2017). Interestingly, NELF-IDR replacements formed condensates even in the absence of any stress (Figures 6E and 6F). Moreover, cells expressing NELFA with FUS- or EWSR1-IDRs showed decreased transcription of tested genes in comparison to NELFA-WT cells under non-stress conditions (Figure 6G), linking NELF condensation to transcriptional reduction. Importantly, cells expressing NELFA-IDR replacements showed significantly better survival upon heat shock in comparison to NELFA-ΔIDR cells (Figure 6H). These observations suggest that the ability of NELF to form condensates is essential for its function in transcriptional downregulation promoting cell survival under stress.

DISCUSSION

Here we report that NELF can form nuclear condensates that are important for transcriptional downregulation and cellular survival under stressful conditions. By increasing local NELF concentration, such condensates may facilitate increased chromatin residence time of NELF. NELF stabilizes promoter-proximally paused Pol II that reduces further transcription initiation (Gressel et al., 2017; Shao and Zeitlinger, 2017), decreasing transcriptional output of target genes during stress. NELF condensates may interact with RNA Pol II at the first pausing step, as reported recently (Aoi et al., 2020). Alternatively, such condensates may sterically prevent the interaction of P-TEFb or other elongation factors with RNA Pol II, ultimately resulting in transcriptional downregulation of the target genes. Additionally, or alternatively, promoter-associated Pol II may dissociate from template DNA and terminate during stress.

At the molecular level, the formation of NELF condensates requires the disordered tentacles in subunits NELFA and NELFE, whose differential sequence compositions likely allow them to engage in intermolecular multivalent interactions (Figure S6G) (Wang et al., 2018). The stress inducibility of NELF condensates may be explained by the fact that most of the P-TEFb phosphorylation sites and more than one-third of all SUMOylation sites lie within the disordered regions (Figures S3D and S4A). Moreover, NELF contains putative SUMO interaction motifs (SIMs) that may further increase the valency of the NELF complex by binding to SUMOylated NELF in the vicinity (Banani et al., 2016; Ditlev et al., 2018; Min et al., 2019). The various layers regulating NELF condensation likely makes it an integrative process that takes place only when multiple independent signaling pathways converge on the NELF complex (Figure 7).

On a more conceptual level, nuclear NELF condensates are similar to cytosolic stress granules. Both condensates are stress-induced and likely formed by phase separation that can be recapitulated *in vitro*. Together, NELF condensates and stress granules are crucial for reversible downregulation of transcription and translation, respectively, thereby repressing gene expression upon stress. It is possible that upstream signaling co-regulates the formation of both these condensates (Samir et al., 2019). In this regard, it is noteworthy that acute translation inhibition blocks stress-induced increase in NELF abundance at chromatin. Our earlier studies reported p38 kinase signaling to be crucial for communication between cytosolic translation events and nuclear transcriptional downregulation under stress conditions (Aprile-Garcia et al., 2019). How stress signaling initiates and/or maintains NELF condensates will be an exciting future avenue (Li et al., 2012; Nott et al., 2015). It is plausible that kinases, phosphatases, or the SUMOylation machinery partition in NELF condensates. The mechanism of CDK9 sequestration upon heat shock in the inactivating complex

deserves further investigation, as CDK9 activity is essential for the upregulation of HSF1 target genes. In addition, it will be important to study how stress activates the SUMO E3 ligase ZNF451.

In summary, we report a stress-induced nuclear condensate, which may contribute to cellular survival strategy under stressful conditions.

STAR★METHODS

Detailed methods are provided in the online version of this paper and include the following:

- KEY RESOURCES TABLE
- RESOURCE AVAILABILITY
  - Lead Contact
  - Materials Availability
  - Data and Code Availability
- EXPERIMENTAL MODEL AND SUBJECT DETAILS
  - Cell Culture
- METHOD DETAILS
  - Cell stress treatments
  - Generating clones
  - Site directed mutagenesis
  - IDR Replacement plasmids
  - Plasmid transfections
  - Cellular fractionation and chromatin extraction
  - Western Blotting
  - Antibodies
  - Cell Imaging
  - Hexanediol Treatment
  - Quantification of nuclear condensates
  - Visualization of chromatin associated endogenous NELFA using immunofluorescence
  - Chemical treatments
  - RNA interference
  - SILAC based Mass-spectrometric analysis of CDK9 interactome and NELFA phosphorylation
  - Chromatin immunoprecipitation and quantitative PCR(qPCR)
  - Quantitative PCR with reverse transcription and nascent-transcript quantification assay
  - *In vitro* SUMO assays
  - RNA Pol II ChIP seq library preparation and data analysis
  - Cell viability assay
  - Expression and purification of full-length NELF and tentacle deletion variants
  - Expression and purification of GFP-NELF tentacle fusion proteins
  - Expression and purification of P-TEFb
  - Fluorescent labeling of NELF complex
  - *In vitro* phase separation assays and microscopy
  - *In vitro* FRAP experiments
  - Real-time P-TEFb droplet phosphorylation
  - Mass spectrometric analysis of P-TEFb phosphorylation sites
  - Analysis of NELF-CTD interaction
  - SLAM-Seq Experiments
  - Bioinformatic analysis
- QUANTIFICATION AND STATISTICAL ANALYSIS

SUPPLEMENTAL INFORMATION

Supplemental Information can be found online at https://doi.org/10.1016/j.molcel.2021.01.016.

ACKNOWLEDGMENTS

We would like to thank UbiQ, M. Timmers, A. Akhtar, S. Leone, R. Collepardo-Guevara, C. Wilson, A. Dejean, S. Carra, and A. Boltendahl for reagents, scientific discussions, and technical assistance and R. Stone for ZNF451 cloning. We also thank Imaging, Proteomics, deep sequencing facilities of Max Planck Institute (MPI) of Immunobiology and Epigenetics, the Facility for Innovative Light Microscopy and the Mass Spectrometry Core Facility of MPI for Biophysical Chemistry for technical assistance and help with data analysis. This work was supported by funds from the Max Planck Society (Germany), the Medical Research Council (UK), and the German Research Foundation (DFG) through the collaborative research center CRC992 (Medical Epigenetics), through the research grant SA 3190, and under Germany's Excellence Strategy EXC-2189 Project ID 390939984 to R.S. P.C. acknowledges support by the Deutsche Forschungsgemeinschaft (SFB860, SPP1935, SPP2191, EXC 2067/1-390729940), the European Research Council (advanced grant TRANSREGULON, grant agreement 693023), and the Volkswagen Foundation. S.M.V. was supported by an EMBO Long-Term Postdoctoral Fellowship (ALTF 745-2014). A.P. is funded by the Max Planck Society and by the European Union's Horizon 2020 research and innovation program under the Marie Skłodowska-Curie grant agreement 765445. J.J.P. acknowledges The Academy of Finland (grant 287336) and The Sigrid Jusélius Foundation.

AUTHOR CONTRIBUTIONS

P.R. and R.S. initiated the project. P.R. performed imaging and molecular cell biology experiments. M.B. designed and performed all *in vitro* experiments. S.M.V. purified recombinant NELF complex. B.H. performed all the computational analysis. F.A.G., A.S.P., A.K., N.E., and E.N. helped with the experiments. J.J.P., A.P., P.C., and R.S. supervised. P.R., M.B., P.C., and R.S. wrote the manuscript with input from all other authors.

DECLARATION OF INTERESTS

The authors declare no competing interests.

Received: March 23, 2020
Revised: October 20, 2020
Accepted: January 11, 2021
Published: February 5, 2021

SUPPORTING CITATIONS

The following reference appears in the supplemental information: King and Jukes, 1969.

REFERENCES

Adelman, K., and Lis, J.T. (2012). Promoter-proximal pausing of RNA polymerase II: emerging roles in metazoans. Nat. Rev. Genet. *13*, 720–731.

Alberti, S., Gladfelter, A., and Mittag, T. (2019). Considerations and Challenges in Studying Liquid-Liquid Phase Separation and Biomolecular Condensates. Cell *176*, 419–434.

Aoi, Y., Smith, E.R., Shah, A.P., Rendleman, E.J., Marshall, S.A., Woodfin, A.R., Chen, F.X., Shiekhattar, R., and Shilatifard, A. (2020). NELF Regulates a Promoter-Proximal Step Distinct from RNA Pol II Pause-Release. Mol Cell *78*, 261–274.

Aprile-Garcia, F., Tomar, P., Hummel, B., Khavaran, A., and Sawarkar, R. (2019). Nascent-protein ubiquitination is required for heat shock-induced gene downregulation in human cells. Nat. Struct. Mol. Biol. *26*, 137–146.

Arrigoni, L., Richter, A.S., Betancourt, E., Bruder, K., Diehl, S., Manke, T., and Bonisch, U. (2016). Standardizing chromatin research: a simple and universal method for ChIP-seq. Nucleic Acids Res *44*, e67.

Banani, S.F., Rice, A.M., Peeples, W.B., Lin, Y., Jain, S., Parker, R., and Rosen, M.K. (2016). Compositional Control of Phase-Separated Cellular Bodies. Cell *166*, 651–663.

Banani, S.F., Lee, H.O., Hyman, A.A., and Rosen, M.K. (2017). Biomolecular condensates: organizers of cellular biochemistry. Nat. Rev. Mol. Cell Biol. *18*, 285–298.

Biamonti, G., and Vourc'h, C. (2010). Nuclear stress bodies. Cold Spring Harb. Perspect. Biol. *2*, a000695.

Boehning, M., Dugast-Darzacq, C., Rankovic, M., Hansen, A.S., Yu, T., Marie-Nelly, H., McSwiggen, D.T., Kokic, G., Dailey, G.M., Cramer, P., et al. (2018). RNA polymerase II clustering through carboxy-terminal domain phase separation. Nat. Struct. Mol. Biol. *25*, 833–840.

Boija, A., Klein, I.A., Sabari, B.R., Dall'Agnese, A., Coffey, E.L., Zamudio, A.V., Li, C.H., Shrinivas, K., Manteiga, J.C., Hannett, N.M., et al. (2018). Transcription Factors Activate Genes through the Phase-Separation Capacity of Their Activation Domains. Cell *175*, 1842–1855.

Chen, F.X., Woodfin, A.R., Gardini, A., Rickels, R.A., Marshall, S.A., Smith, E.R., Shiekhattar, R., and Shilatifard, A. (2015). PAF1, a Molecular Regulator of Promoter-Proximal Pausing by RNA Polymerase II. Cell *162*, 1003–1015.

Chen, S., Zhou, Y., Chen, Y., and Gu, J. (2018). fastp: an ultra-fast all-in-one FASTQ preprocessor. Bioinformatics *34*, i884–i890.

Cho, W.K., Spille, J.H., Hecht, M., Lee, C., Li, C., Grube, V., and Cisse, I.I. (2018). Mediator and RNA polymerase II clusters associate in transcription-dependent condensates. Science *361*, 412–415.

Core, L., and Adelman, K. (2019). Promoter-proximal pausing of RNA polymerase II: a nexus of gene regulation. Genes Dev. *33*, 960–982.

Core, L.J., Waterfall, J.J., and Lis, J.T. (2008). Nascent RNA sequencing reveals widespread pausing and divergent initiation at human promoters. Science *322*, 1845–1848.

Cotto, J., Fox, S., and Morimoto, R. (1997). HSF1 granules: a novel stress-induced nuclear compartment of human cells. J. Cell Sci. *110*, 2925–2934.

Cox, J., and Mann, M. (2008). MaxQuant enables high peptide identification rates, individualized p.p.b.-range mass accuracies and proteome-wide protein quantification. Nat. Biotechnol. *26*, 1367–1372.

Cramer, P. (2019). Organization and regulation of gene transcription. Nature *573*, 45–54.

Ditlev, J.A., Case, L.B., and Rosen, M.K. (2018). Who's In and Who's Out-Compositional Control of Biomolecular Condensates. J. Mol. Biol. *430*, 4666–4684.

Eick, D., and Geyer, M. (2013). The RNA polymerase II carboxy-terminal domain (CTD) code. Chem. Rev. *113*, 8456–8490.

Eisenhardt, N., Chaugule, V.K., Koidl, S., Droescher, M., Dogan, E., Rettich, J., Sutinen, P., Imanishi, S.Y., Hofmann, K., Palvimo, J.J., and Pichler, A. (2015). A new vertebrate SUMO enzyme family reveals insights into SUMO-chain assembly. Nat. Struct. Mol. Biol. *22*, 959–967.

Gibson, G. (2008). The environmental contribution to gene expression profiles. Nat. Rev. Genet. *9*, 575–581.

Gibson, B.A., Doolittle, L.K., Schneider, M.W.G., Jensen, L.E., Gamarra, N., Henry, L., Gerlich, D.W., Redding, S., and Rosen, M.K. (2019). Organization of Chromatin by Intrinsic and Regulated Phase Separation. Cell *179*, 470–484.

Gressel, S., Schwalb, B., Decker, T.M., Qin, W., Leonhardt, H., Eick, D., and Cramer, P. (2017). CDK9-dependent RNA polymerase II pausing controls transcription initiation. eLife *6*, e29736.

Gressel, S., Schwalb, B., and Cramer, P. (2019). The pause-initiation limit restricts transcription activation in human cells. Nat. Commun. *10*, 3603.

Gu, Z., Eils, R., and Schlesner, M. (2016). Complex heatmaps reveal patterns and correlations in multidimensional genomic data. Bioinformatics *32*, 2847–2849.

Guo, Y.E., Manteiga, J.C., Henninger, J.E., Sabari, B.R., Dall'Agnese, A., Hannett, N.M., Spille, J.H., Afeyan, L.K., Zamudio, A.V., Shrinivas, K., et al. (2019). Pol II phosphorylation regulates a switch between transcriptional and splicing condensates. Nature *572*, 543–548.

Harlen, K.M., and Churchman, L.S. (2017). The code and beyond: transcription regulation by the RNA polymerase II carboxy-terminal domain. Nat. Rev. Mol. Cell Biol. *18*, 263–273.

Harrison, A.F., and Shorter, J. (2017). RNA-binding proteins with prion-like domains in health and disease. Biochem. J. *474*, 1417–1438.

Hendriks, I.A., Lyon, D., Young, C., Jensen, L.J., Vertegaal, A.C., and Nielsen, M.L. (2017). Site-specific mapping of the human SUMO proteome reveals co-modification with phosphorylation. Nat. Struct. Mol. Biol. *24*, 325–336.

Hendriks, I.A., Lyon, D., Su, D., Skotte, N.H., Daniel, J.A., Jensen, L.J., and Nielsen, M.L. (2018). Site-specific characterization of endogenous SUMOylation across species and organs. Nat. Commun. *9*, 2456.

Herzog, V.A., Reichholf, B., Neumann, T., Rescheneder, P., Bhat, P., Burkard, T.R., Wlotzka, W., von Haeseler, A., Zuber, J., and Ameres, S.L. (2017). Thiol-linked alkylation of RNA to assess expression dynamics. Nat. Methods *14*, 1198–1204.

Hnisz, D., Shrinivas, K., Young, R.A., Chakraborty, A.K., and Sharp, P.A. (2017). A Phase Separation Model for Transcriptional Control. Cell *169*, 13–23.

Holcik, M., and Sonenberg, N. (2005). Translational control in stress and apoptosis. Nat. Rev. Mol. Cell Biol. *6*, 318–327.

Hyman, A.A., Weber, C.A., and Jülicher, F. (2014). Liquid-liquid phase separation in biology. Annu. Rev. Cell Dev. Biol. *30*, 39–58.

Jonkers, I., and Lis, J.T. (2015). Getting up to speed with transcription elongation by RNA polymerase II. Nat. Rev. Mol. Cell Biol. *16*, 167–177.

King, J.L., and Jukes, T.H. (1969). Non-Darwinian evolution. Science *164*, 788–798.

Knipscheer, P., Flotho, A., Klug, H., Olsen, J.V., van Dijk, W.J., Fish, A., Johnson, E.S., Mann, M., Sixma, T.K., and Pichler, A. (2008). Ubc9 sumoylation regulates SUMO target discrimination. Mol Cell *31*, 371–382.

Kroschwald, S., Maharana, S., and Simon, A. (2017). Hexanediol: a chemical probe to investigate the material properties of membrane-less compartments. Matters. https://doi.org/10.19185/matters.201702000010.

Kwak, H., and Lis, J.T. (2013). Control of transcriptional elongation. Annu. Rev. Genet. *47*, 483–508.

Kwon, I., Kato, M., Xiang, S., Wu, L., Theodoropoulos, P., Mirzaei, H., Han, T., Xie, S., Corden, J.L., and McKnight, S.L. (2013). Phosphorylation-regulated binding of RNA polymerase II to fibrous polymers of low-complexity domains. Cell *155*, 1049–1060.

Langmead, B., and Salzberg, S.L. (2012). Fast gapped-read alignment with Bowtie 2. Nat Methods *9*, 357–359.

Li, P., Banjade, S., Cheng, H.C., Kim, S., Chen, B., Guo, L., Llaguno, M., Hollingsworth, J.V., King, D.S., Banani, S.F., et al. (2012). Phase transitions in the assembly of multivalent signalling proteins. Nature *483*, 336–340.

Liao, Y., Smyth, G.K., and Shi, W. (2014). featureCounts: an efficient general purpose program for assigning sequence reads to genomic features. Bioinformatics *30*, 923–930.

Love, M.I., Huber, W., and Anders, S. (2014). Moderated estimation of fold change and dispersion for RNA-seq data with DESeq2. Genome Biol *15*, 550.

Lu, X., Zhu, X., Li, Y., Liu, M., Yu, B., Wang, Y., Rao, M., Yang, H., Zhou, K., Wang, Y., et al. (2016). Multiple P-TEFbs cooperatively regulate the release of promoter-proximally paused RNA polymerase II. Nucleic Acids Res. *44*, 6853–6867.

Lu, H., Yu, D., Hansen, A.S., Ganguly, S., Liu, R., Heckert, A., Darzacq, X., and Zhou, Q. (2018). Phase-separation mechanism for C-terminal hyperphosphorylation of RNA polymerase II. Nature *558*, 318–323.

Mahat, D.B., Salamanca, H.H., Duarte, F.M., Danko, C.G., and Lis, J.T. (2016). Mammalian Heat Shock Response and Mechanisms Underlying Its Genome-wide Transcriptional Regulation. Mol. Cell *62*, 63–78.

Marshall, N.F., and Price, D.H. (1995). Purification of P-TEFb, a transcription factor required for the transition into productive elongation. J. Biol. Chem. *270*, 12335–12338.

Min, J., Wright, W.E., and Shay, J.W. (2019). Clustered telomeres in phase-separated nuclear condensates engage mitotic DNA synthesis through BLM and RAD52. Genes Dev. *33*, 814–827.

Molliex, A., Temirov, J., Lee, J., Coughlin, M., Kanagaraj, A.P., Kim, H.J., Mittag, T., and Taylor, J.P. (2015). Phase separation by low complexity domains promotes stress granule assembly and drives pathological fibrillization. Cell *163*, 123–133.

Narita, T., Yamaguchi, Y., Yano, K., Sugimoto, S., Chanarat, S., Wada, T., Kim, D.K., Hasegawa, J., Omori, M., Inukai, N., et al. (2003). Human transcription elongation factor NELF: identification of novel subunits and reconstitution of the functionally active complex. Mol. Cell. Biol. *23*, 1863–1873.

Neumann, T., Herzog, V.A., Muhar, M., von Haeseler, A., Zuber, J., Ameres, S.L., and Rescheneder, P. (2019). Quantification of experimentally induced nucleotide conversions in high-throughput sequencing datasets. BMC Bioinformatics *20*, 258.

Nguyen, V.T., Kiss, T., Michels, A.A., and Bensaude, O. (2001). 7SK small nuclear RNA binds to and inhibits the activity of CDK9/cyclin T complexes. Nature *414*, 322–325.

Niskanen, E.A., Malinen, M., Sutinen, P., Toropainen, S., Paakinaho, V., Vihervaara, A., Joutsen, J., Kaikkonen, M.U., Sistonen, L., and Palvimo, J.J. (2015). Global SUMOylation on active chromatin is an acute heat stress response restricting transcription. Genome Biol. *16*, 153.

Nott, T.J., Petsalaki, E., Farber, P., Jervis, D., Fussner, E., Plochowietz, A., Craggs, T.D., Bazett-Jones, D.P., Pawson, T., Forman-Kay, J.D., and Baldwin, A.J. (2015). Phase transition of a disordered nuage protein generates environmentally responsive membraneless organelles. Mol. Cell *57*, 936–947.

Oellerich, T., Grønborg, M., Neumann, K., Hsiao, H.H., Urlaub, H., and Wienands, J. (2009). SLP-65 phosphorylation dynamics reveals a functional basis for signal integration by receptor-proximal adaptor proteins. Mol. Cell. Proteomics *8*, 1738–1750.

Ong, S.E., Blagoev, B., Kratchmarova, I., Kristensen, D.B., Steen, H., Pandey, A., and Mann, M. (2002). Stable isotope labeling by amino acids in cell culture, SILAC, as a simple and accurate approach to expression proteomics. Mol. Cell. Proteomics *1*, 376–386.

Palozola, K.C., Donahue, G., Liu, H., Grant, G.R., Becker, J.S., Cote, A., Yu, H., Raj, A., and Zaret, K.S. (2017). Mitotic transcription and waves of gene reactivation during mitotic exit. Science *358*, 119–122.

Park, S.S., Wu, W.W., Zhou, Y., Shen, R.F., Martin, B., and Maudsley, S. (2012). Effective correction of experimental errors in quantitative proteomics using stable isotope labeling by amino acids in cell culture (SILAC). J Proteomics *75*, 3720–3732.

Peng, K., Radivojac, P., Vucetic, S., Dunker, A.K., and Obradovic, Z. (2006). Length-dependent prediction of protein intrinsic disorder. BMC Bioinformatics *7*, 208.

Pichler, A. (2008). Analysis of sumoylation. Methods Mol Biol *446*, 131–138.

Pichler, A., Knipscheer, P., Saitoh, H., Sixma, T.K., and Melchior, F. (2004). The RanBP2 SUMO E3 ligase is neither HECT- nor RING-type. Nat Struct Mol Biol *11*, 984–991.

Portz, B., Lu, F., Gibbs, E.B., Mayfield, J.E., Rachel Mehaffey, M., Zhang, Y.J., Brodbelt, J.S., Showalter, S.A., and Gilmour, D.S. (2017). Structural heterogeneity in the intrinsically disordered RNA polymerase II C-terminal domain. Nat. Commun. *8*, 15231.

Price, D.H. (2000). P-TEFb, a cyclin-dependent kinase controlling elongation by RNA polymerase II. Mol. Cell. Biol. *20*, 2629–2634.

Quinlan, A.R., and Hall, I.M. (2010). BEDTools: a flexible suite of utilities for comparing genomic features. Bioinformatics *26*, 841–842.

Ramirez, F., Ryan, D.P., Gruning, B., Bhardwaj, V., Kilpert, F., Richter, A.S., Heyne, S., Dundar, F., and Manke, T. (2016). deepTools2: a next generation web server for deep-sequencing data analysis. Nucleic Acids Res *44*, W160–165.

Sabari, B.R., Dall'Agnese, A., Boija, A., Klein, I.A., Coffey, E.L., Shrinivas, K., Abraham, B.J., Hannett, N.M., Zamudio, A.V., Manteiga, J.C., et al. (2018). Coactivator condensation at super-enhancers links phase separation and gene control. Science *361*, eaar3958.

Sahin, U., Ferhi, O., Jeanne, M., Benhenda, S., Berthier, C., Jollivet, F., Niwa-Kawakita, M., Faklaris, O., Setterblad, N., de Thé, H., and Lallemand-Breitenbach, V. (2014). Oxidative stress-induced assembly of PML nuclear bodies controls sumoylation of partner proteins. J. Cell Biol. *204*, 931–945.

Samir, P., Kesavardhana, S., Patmore, D.M., Gingras, S., Malireddi, R.K.S., Karki, R., Guy, C.S., Briard, B., Place, D.E., Bhattacharya, A., et al. (2019). DDX3X acts as a live-or-die checkpoint in stressed cells by regulating NLRP3 inflammasome. Nature *573*, 590–594.

Shao, W., and Zeitlinger, J. (2017). Paused RNA polymerase II inhibits new transcriptional initiation. Nat. Genet. *49*, 1045–1051.

Shin, Y., and Brangwynne, C.P. (2017). Liquid phase condensation in cell physiology and disease. Science *357*, eaaf4382.

Spradling, A., Penman, S., and Pardue, M.L. (1975). Analysis of Drosophila mRNA by in situ hybridization: sequences transcribed in normal and heat shocked cultured cells. Cell *4*, 395–404.

Vihervaara, A., Mahat, D.B., Guertin, M.J., Chu, T., Danko, C.G., Lis, J.T., and Sistonen, L. (2017). Transcriptional response to stress is pre-wired by promoter and enhancer architecture. Nat. Commun. *8*, 255.

Vos, S.M., Pöllmann, D., Caizzi, L., Hofmann, K.B., Rombaut, P., Zimniak, T., Herzog, F., and Cramer, P. (2016). Architecture and RNA binding of the human negative elongation factor. eLife *5*, e14981.

Vos, S.M., Farnung, L., Boehning, M., Wigge, C., Linden, A., Urlaub, H., and Cramer, P. (2018a). Structure of activated transcription complex Pol II-DSIF-PAF-SPT6. Nature *560*, 607–612.

Vos, S.M., Farnung, L., Urlaub, H., and Cramer, P. (2018b). Structure of paused transcription complex Pol II-DSIF-NELF. Nature *560*, 601–606.

Wada, T., Takagi, T., Yamaguchi, Y., Ferdous, A., Imai, T., Hirose, S., Sugimoto, S., Yano, K., Hartzog, G.A., Winston, F., et al. (1998). DSIF, a novel transcription elongation factor that regulates RNA polymerase II processivity, is composed of human Spt4 and Spt5 homologs. Genes Dev. *12*, 343–356.

Wang, J., Choi, J.M., Holehouse, A.S., Lee, H.O., Zhang, X., Jahnel, M., Maharana, S., Lemaitre, R., Pozniakovsky, A., Drechsel, D., et al. (2018). A Molecular Grammar Governing the Driving Forces for Phase Separation of Prion-like RNA Binding Proteins. Cell *174*, 688–699.

Warnes, G.R. (2012). gplots: Various R programming tools for plotting data.

Wei, P., Garber, M.E., Fang, S.M., Fischer, W.H., and Jones, K.A. (1998). A novel CDK9-associated C-type cyclin interacts directly with HIV-1 Tat and mediates its high-affinity, loop-specific binding to TAR RNA. Cell *92*, 451–462.

Wickham, H. (2016). ggplot2: Elegant Graphics for Data Analysis (New York: Springer-Verlag).

Yamaguchi, Y., Takagi, T., Wada, T., Yano, K., Furuya, A., Sugimoto, S., Hasegawa, J., and Handa, H. (1999). NELF, a multisubunit complex containing RD, cooperates with DSIF to repress RNA polymerase II elongation. Cell *97*, 41–51.

Yang, Z., Zhu, Q., Luo, K., and Zhou, Q. (2001). The 7SK small nuclear RNA inhibits the CDK9/cyclin T1 kinase to control transcription. Nature *414*, 317–322.

Zhang, Y., Liu, T., Meyer, C.A., Eeckhoute, J., Johnson, D.S., Bernstein, B.E., Nusbaum, C., Myers, R.M., Brown, M., Li, W., et al. (2008). Model-based analysis of ChIP-Seq (MACS). Genome Biol *9*, R137.

Zhou, Y., Zhou, B., Pache, L., Chang, M., Khodabakhshi, A.H., Tanaseichuk, O., Benner, C., and Chanda, S.K. (2019). Metascape provides a biologist-oriented resource for the analysis of systems-level datasets. Nat. Commun. *10*, 1523.

STAR★METHODS

KEY RESOURCES TABLE

REAGENT or RESOURCE	SOURCE	IDENTIFIER
Antibodies		
Goat polyclonal anti-NELF-A (A-20)	Santa Cruz	Cat#sc-23599; RRID: AB_2241683
Rabbit polyclonal anti-NELF-E (H-140)	Santa Cruz	Cat#sc-32912; RRID: AB_2177858
Mouse monoclonal anti-NELF-D (C-10)	Santa Cruz	Cat#sc-393972; RRID: AB_2847956
Rabbit polyclonal anti-Histone H3	Abcam	Cat#ab70550; RRID: AB_1209471
Rabbit polyclonal anti-SNRNP70	Abcam	Cat#ab83306; RRID: AB_10673827
Rabbit polyclonal anti-ZNF451	Bethyl Laboratories inc	Cat#A305-177A; RRID: AB_2631570
Rabbit polyclonal anti-RPB3	Millipore	Cat#ABE999
Mouse monoclonal SUMO2/3	Andrea Pichler Lab	8A2
Rabbit monoclonal anti-PML	Abcam	Cat#ab179466
Bacterial and Virus Strains		
E. coli BL21 (DE3) cells	Agilent	Cat#230245
Chemicals, Peptides, and Recombinant Proteins		
Tetracycline	Sigma-Aldrich	Cat#T7660
Blasticidin S	Carl Roth	Cat#CP14.1
Hygromycin B	Thermo Fisher Scientific	Cat#10687010
1,6-hexanediol	Sigma-Aldrich	Cat#240117-50G
SUMO E1 inhibitor ML-792	UbiQ	N/A
Arsenic(III) oxide	Sigma-Aldrich	Cat#202673-5G
DAPI	SERVA	Cat#18860
DMEM	Sigma-Aldrich	Cat#D5671
DMSO	Sigma-Aldrich	Cat#41639
Fetal Bovine Serum	Sigma-Aldrich	Cat#F0804
L-Glutamine	Sigma-Aldrich	Cat#G7513
Penicillin Streptomycin	Sigma-Aldrich	Cat#P4333
TRI-Reagent	Sigma-Aldrich	Cat#T9424
Trypsin	Promega	Cat#V5113
Zeocin	Invitrogen	Cat#R25001
Restriction enzyme XhoI	New England BioLabs	Cat#R0146S
Restriction enzyme HindIII-HF	New England BioLabs	Cat#R3104S
Phosphate Buffer Saline (PBS)	Sigma-Aldrich	Cat#D8537
4% fomaldehyde fixative solution	Invitrogen	Cat#FB002
16% methanol-free formaldehyde	Applichem	Cat#A3832
Proteinase K	Sigma-Aldrich	Cat#P2308
RNase A	Applichem	Cat#3832
Isopropyl β-d-1-thiogalactopyranoside (IPTG)	Carl Roth	Cat#2316.4
N-terminally carboxyfluorescein (FAM)-labeled CTD peptides	PSL GmbH	N/A
Critical Commercial Assays		
CellTiter-Glo 2 Luminescent Cell Viability Assay	Promega	Cat#G7570
GFP-trap magnetic agarose beads	ChromoTek	Cat#gtma 20
Lipofectamine 3000	Thermo Fisher	Cat#L3000-015
Lipofectamine RNAiMax	Thermo Fisher	Cat#13778150
PrimeScript RT Reagent Kit with gDNA Erase	Takara Bio Science	Cat#RR047

(*Continued on next page*)

Continued

REAGENT or RESOURCE	SOURCE	IDENTIFIER
TB Green Premix Ex Taq	Takara Bio Science	Cat#RR420
Q5 Hot Start High-Fidelity DNA polymerase	New England BioLabs	Cat#M0493S
Gibson assembly kit	New England BioLabs	Cat#E5510S
TFP-Alexa Fluor 488 dye	Molecular Probes	Cat#A37570
Deposited Data		
Deep sequencing data	This paper	GSE140053
NelfA/E ChIP-seq data (NHS and HS)	Aprile Garcia et. al. 2019	N/A
RNA Pol II ChIP-seq data (NHS and HS)	Aprile Garcia et. al. 2019	N/A
RNA Pol II ChIP-seq data (siNON and siUBE2I)	Niskanen et. al. 2015	N/A
Experimental Models: Cell Lines		
Human: Flp-In T-Rex HEK293	Renato Paro, ETH Zurich, Switzerland	N/A
Human: Flp-In T-Rex HeLa	Marc Timmers, Freiburg	N/A
HeLa Flp-In T-Rex NELFA-cGFP cells	This study	N/A
HeLa Flp-In T-Rex NELFC/D-cGFP cells	This study	N/A
HEK293 Flp-In T-Rex NELFA-cGFP cells	This study	N/A
HEK293 Flp-In T-Rex CDK9-cGFP cells	This study	N/A
HeLa Flp-In T-Rex GFP cells	This study	N/A
T. ni High Five insect cell line	Expression Systems	BTI-TN-5B1-4
Oligonucleotides		
Refer to Table S1 for Primer Sequences	N/A	N/A
SMARTpool: ON_TARGETplus ZNF451 siRNA	Dharmacon	M-013935-01
SMARTpool: ON_TARGETplus UBE2I siRNA	Dharmacon	L-004910-00
PIAS1 siGenome siRNA	Origene	SR305620
PIAS4 siGenome siRNA	Origene	SR309861
siGenome Nontargeting siRNA	Dharmacon	D-001206-13
siRNA 3′UTR NELFA (Custom designed)	Microsynth	N/A
SMARTpool: ON_TARGETplus PML siRNA	Dharmacon	M-006547-01
Recombinant DNA		
pOG44	Renato Paro, ETH Zurich, Switzerland	N/A
pDEST-mCherry-N1	Addgene	31907
pDEST+cGFP	Marc Timmers, Freiburg	N/A
pDEST+bgGFP	Marc Timmers, Freiburg	N/A
pDEST+3FHBH-GFP	This Paper	N/A
pDEST+CDK9-cGFP	This Paper	N/A
pDEST+NELFA-cGFP	This Paper	N/A
pDEST+NELFA-bgGFP	This Paper	N/A
pDEST+NELFE-cGFP	This Paper	N/A
pDEST+NELFE-mCherry	This Paper	N/A
pDEST+NELFC/D-cGFP	This Paper	N/A
pDEST+NELFC/D-mCherry	This Paper	N/A
pDEST+NELFA-mCherry	This Paper	N/A
pDEST+NELFA-dIDR-mCherry	This Paper	N/A
pDEST+NELFA-dIDR-fusion-FUS-IDR-mCherry	This Paper	N/A
pDEST+NELFA-dIDR- fusion-EWSR1-IDR-mCherry	This Paper	N/A
pDEST+CCNT1-cGFP	This Paper	N/A

(*Continued on next page*)

Continued

REAGENT or RESOURCE	SOURCE	IDENTIFIER
pET+EGFP-NELFA(189-528)	This paper	N/A
pET+EGFP-NELFE(139-380)	This paper	N/A
pET+NELFE(139-380)-EGFP-NELFA(189-528)	This paper	N/A
pFastBac+NELFA,-B,-D,-E	Vos et al., 2018b	N/A
pFastBac+NELFA(1-188),-B,-D,-E	Vos et al., 2018b	N/A
pFastBac+NELFA,-B,-D,-E(1-138)	Vos et al., 2018b	N/A
pET+MBP-hCTD	Boehning et al., 2018	N/A
pET+MBP-yCTD	Boehning et al., 2018	N/A
pET+MBP-distal hCTD	This paper	N/A
pCruz+GFP-ZNF451-1	Andrea Pichler Lab	N/A
Software and Algorithms		
Metascape	Zhou et al., 2019	https://metascape.org/gp/index.html#/main/step1
featureCounts	Liao et al., 2014	http://www.rdocumentation.org/packages/Rsubread/versions/1.22.2
DESeq2	Love et al., 2014	https://bioconductor.org/packages/release/bioc/html/DESeq2.html
vioplot	N/A	https://github.com/TomKellyGenetics/vioplot
ggplot2	Wickham, 2016	https://ggplot2.tidyverse.org
Imaris	Imaris 9.1 and Imaris 9.3	https://imaris.oxinst.com/packages
Bowtie2	Langmead and Salzberg, 2012	https://github.com/BenLangmead/bowtie2
MACS2	Zhang et al., 2008	https://github.com/macs3-project/MACS
bedtools2	Quinlan and Hall, 2010	https://bedtools.readthedocs.io/en/latest/
GraphPad Prism	GraphPad Software	https://www.graphpad.com
deeptools2	Ramirez et al., 2016	https://deeptools.readthedocs.io/en/develop
R Statistical Computing Software	N/A	https://www.r-project.org
gplots	Warnes, 2012	https://www.rdocumentation.org/packages/gplots/versions/3.0.1.1
MaxQuant version 1.5.7.4	Cox and Mann, 2008	https://www.maxquant.org
MaxQuant version 1.5.2.8)	Cox and Mann, 2008	https://www.maxquant.org
Perseus version 1.5.2.4	N/A	N/A
FlowJo	FLOWJO LLC	https://www.flowjo.com/
FIJI version 1.52 h	N/A	https://imagej.net/Fiji
IGV	N/A	http://software.broadinstitute.org/software/igv/
SlamDunk v0.3.4	Neumann et al., 2019	https://t-neumann.github.io/slamdunk/
ComplexHeatmap	Gu et al., 2016	http://bioconductor.org/packages/release/bioc/html/ComplexHeatmap.html

RESOURCE AVAILABILITY

Lead Contact

Further information and requests for resources and reagents should be directed to and will be fulfilled by the Lead Contact, Ritwick Sawarkar (rs2099@cam.ac.uk).

Materials Availability

All reagents generated in this study can be requested without restriction upon an agreement with a material transfer agreement (MTA).

Data and Code Availability

All deep-sequencing data generated in this study are deposited in GEO and are available under accession number GEO: GSE140053.

EXPERIMENTAL MODEL AND SUBJECT DETAILS

Cell Culture

HeLa Flp-In T-Rex cells (obtained from M. Timmers, University of Freiburg) and HEK293 Flp-In T-Rex cells (Obtained from R. Paro, ETH Zurich) were cultured in DMEM high glucose medium supplemented with 10% FBS (Sigma-Aldrich F0804), 2mM L-glutamine (Sigma-Aldrich, G7513) and 1% penicillin-streptomycin (Sigma-Aldrich, P4333). Cells were kept at 37°C in 5% CO_2 incubator. All cell lines were routinely checked for mycoplasma contamination by PCR.

METHOD DETAILS

Cell stress treatments

Heat shock experiments were performed by moving tissue culture plates with growing cells from a 37°C incubator to a 43°C incubator for 30 min, unless stated otherwise.

Heat shock recovery experiments are performed by moving tissue culture plates to a 37°C incubator after heat shock treatment for mentioned time durations. To induce heavy metal stress, the cells were treated with 100 μM arsenic trioxide for 1 h.

Generating clones

For generation of clones for human proteins, hORFs in pDONOR vector were purchased from BIOSS, University of Freiburg and Cloned into GFP (kind gift from Marc Timmers, University of Freiburg) or mCherry (Addgene 31907) pDestination vector using Gateway LR clonase II enzyme kit (Life Technologies 11791020).

Site directed mutagenesis

The primers to introduce deletions were designed using NEBaseChanger. The NELFA mutants were generated using full plasmid amplification of WT plasmid with primers for deletions mutations. The Q5 Hot Start High-Fidelity DNA polymerase was used to perform PCR amplifications according to manufacturer's instructions (New England BioLabs, M0494S). PCR products were subjected to DpnI digestion to remove co-purifed parental plasmid DNA. Colonies were selected with appropriate antibiotic selection marker and sequenced to confirm the deletions.

IDR Replacement plasmids

The NELFA-mCherry dIDR construct was used for genrating IDR replacement mutants.

XhoI and HindIII restriction sites separated by Gly-Ser-Ser codons were inserted at the end of NELFA-dIDR mutant using Q5 Hot Start High-Fidelity DNA polymerase. The insertion of restriction sites was confirmed with double restriction digestion and sequencing. The IDR regions from FUS (aa 61- 260) and EWSR1 (aa 121-340) were amplied from pDonor vectors with primers containing restriction sites and were ligated in the modified NELFA-dIDR plasmid using restriction enzymes based cloning. The cloning was confirmed with sequencing the plasmids.

Plasmid transfections

HEK293 and HeLa cells were transfected with Lipofectamine 3000 (Life Technologies, L3000) according to the manufacturer's instructions. mCherry tag containing vectors, CDK9-cGFP, CCNT1-cGFP and ZNF451-GFP vectors were transiently transfected in HeLa cells. NELFA-cGFP, NELFA-BG-nGFP, GFP-3FHBH (kind gift from Timmers lab, Freiburg and Akhtar Department, MPI Freiburg) were stably transfected in Flp-In T-Rex HeLa cells grown in 100 μg/mL Zeocin (Invitrogen, R25001) for at least three days before transfection. Stable positive clones were selected for at least three weeks in 15 μg/mL blasticidin S (Carl Roth CP14.1) and 100 μg/mL hygromycin B (Thermo Fisher Scientific, 10687010). Expression of proteins was induced with 1 μg/mL tetracycline (Sigma-Aldrich, T7660).

Cellular fractionation and chromatin extraction

Cells were harvested by scrapping and washing twice in ice-cold 1xPBS. Total cell extracts for western blot analysis were obtained by lysing cells in lysis buffer (50 mM Tris-HCl, pH 6.8, 2% SDS and 10% glycerol). Chromatin extraction was done as described previously (Aprile-Garcia et al., 2019). Briefly, cells were washed twice with ice-cold PBS and an aliquot was removed and saved as whole cell extract. Remaining cells were resuspended in buffer A (10 mM HEPES, pH 7.9, 5 mM $MgCl_2$, 0.25cM sucrose) and incubated on ice for 5 min. Cells were passed through 18 G needles five times and centrifuged at 2,000 g for 10 min at 4°C. The nuclear pellet was washed with buffer A, resuspended in 0.5 M buffer B (20 mM HEPES, pH 7.9, 0.5 M KCl, 1.5 mM $MgCl_2$, 0.1 mM EDTA, 10% glycerol) and incubated on a rotator for 30 min at 4°C. The suspension was centrifuged and the chromatin pellet was resuspended in 2 M buffer B (20 mM HEPES, pH 7.9, 2 M KCl, 1.5 mM $MgCl_2$, 0.1 mM EDTA, 10% glycerol), passed through a 200 μL cut tip ten times and incubated while rotating for 30 min at 4 °C. Chromatin fractions were sonicated for 15 cycles (30 s on, 30 s off, high power) in a Bioruptor sonication device. Samples were centrifuged at 20,000 g for 30 min to remove debris and unsonicated material.

Western Blotting

The whole cell lysates or chromatin fractions were prepared in buffers mentioned aboved. Samples were mixed in 3:1 ratio with 4x protein loading buffer (200 mM Tris-HCl pH 6.8, 8% SDS, 40% glycerol, 0.2% bromophenol blue and 20% Beta-mercaptoethanol) and boiled for 10 min at 95°C. Tris-glycine-based denaturing SDS-polyacrylamide gel electrophoresis was used before standard western blot procedures.

Antibodies

SUMO hybridoma SUMO2 8A2, were procured from Developmental Studies Hybridoma Bank, created by the NICHD of the NIH and maintained at The University of Iowa, Department of Biology (http://dshb.biology.uiowa.edu/) and supernatant was produced in Pichler lab. The SUMO2 antisera were used at 1:100. All other primary antibodies were purchased and validated by the manufacturers (data available on manufacturers' websites). They were used at the indicated dilutions; anti-NELFA (goat polyclonal, sc-23599 (A-20), Santa Cruz Biotechnology) at 1:1,000, anti-NELFC/D (mouse monoclonal, sc-393972 (C-10), Santa Cruz Biotechnology) 1:1,000, anti-NELFE (rabbit polyclonal, sc-32912 (H-140), Santa Cruz Biotechnology) at 1:1,000, anti-SNRNP70 (rabbit polyclonal, ab83306, Abcam) at 1:1,000, anti-ZNF451 (rabbit polyclonal, A305-177A, Bethyl Laboratories inc), anti-RPB3 (rabbit polyclonal, ABE999, Millipore) at 1:1,000, and anti-Histone H3 (rabbit polyclonal, ab70550, Abcam) at 1:5,000. Secondary antibodies against goat, rabbit or mouse proteins were horseradish peroxidase conjugated and were typically used at 1:10,000 dilution. Anti-rabbit (NA934V) and anti-mouse (NA931V) antibodies were purchased from GE healthcare. Anti-goat (sc-2354) antibody was purchased from Santa Cruz Biotechnology.

Cell Imaging

Cells were grown on Nunc Lab-Tek 8 well chambers (Thermo Fisher 155411) 24 h at 37 °C and then either transfected with mCherry constructs using Lipofectamine 3000 (Life Technologies, L3000) or induced with 1 μg/mL tetracycline (Sigma-Aldrich, T7660) for Flp-In T-rex stable cell lines. Cells were either left at 37°C (No Heat Shock, NHS) or shifted to 43°C incubator for indicated time periods (Heat shock, HS).

For live cell imaging, samples were taken immediately to microscope with temperature- and CO_2- controlled stage top incubation unit (Tokai Hit).

For fixed cell imaging, cells were treated with 4% fomaldehyde fixative solution (Invitrogen, FB002) for 10 min at 37°C post treatments and washed three times with 1xPBS (Sigma-Aldrich D8537). DAPI is added for 30 min at room temperature in 1xPBS and images were acquired with a Zeiss LSM780 confocal microscope using 63x oil immersion objective at a zoom range 0.6-2x. Z stacks were recorded and collapsed into a single maximum intensity projection using Zen black software. Images were processed using Zen blue or Imaris. For transient transfections, images were acquired with laser powers to avoid saturation. Images were presented as Min/Max intensity or Best fit function of Zen blue software.

Colocalization images for NELFA-NELFE were acquired using Airyscan LSM880 microscope using 63x objective with oil immersion. The images were processed in Airyscan itself with default settings and using Zen blue subsequently.

Hexanediol Treatment

Cells were plated Nunc Lab-Tek Chamber Slides in 400 μl complete media in 4 different sets and induced with 1 ug/mL tetracycline in fresh media for 24 h. Cells were either left at 37°C with or without 10% 1,6-hexanediol treatment for 15 min (NHS and NHS + Hex) or shifted to a 43°C incubator with or without 10% 1,6-hexanediol treatment for 15 min (HS and HS + Hex). Cells were harvested, fixed and imaged as described above using a Zeiss LSM780 confocal microscope.

Quantification of nuclear condensates

For counting number of cells with heat shock induced puncta, minimum of two individual replicates were performed on different days and cells showing condensates were counted. Mean value with standard deviation from two replicates was reported. For counting number of condensates per cell a minimum of two individual replicates were done on different days. The number of condensates per nucleus was determined using Imaris software (version 9.3) in batch analysis mode with Cells module with custom parameters. One of the two representative replicates is presented for each condition with their mean and standard deviation. The number of condensates for NHS conditions were counted manually given the few number of condensates per cell. Sphericity of the condensates was measured using Imaris software (version 9.1) with Surface module with custom parameters.

Visualization of chromatin associated endogenous NELFA using immunofluorescence

Cells were plated Nunc Lab-Tek Chamber Slides in 400 μl complete media in 4 different sets and induced with 1 μg/mL tetracycline in fresh media for 24 h. Cells were either left at 37°C (NHS) or shifted to a 43°C incubator (HS) for 30 min. Cells were washed once with ice cold 1x PBS and then incubated with 0.2% Triton X-100 for 6 min on ice. Cells were washed twice with ice cold 1x PBS and 200 ul of 4% fomaldehyde fixative solution (Invitrogen, FB002) was added for 10 min at 37°C. Cells were washed twice with ice cold 1x PBS and 0.4% Triton X-100 was added for 15 min at room temperature. Cells were washed and blocked with 5% BSA solution in 1x PBS for 2 h at room temperature. Blocking solution was removed and cells were incubated with primary antibody anti-NELFA (goat polyclonal, sc-23599 (A-20), Santa Cruz Biotechnology) at 1:100 dilution overnight at 4°C incubator. Cells were washed thrice with 1x PBS

and labeled secondary antibody was added for 2 h at room temperature. Cells were washed thrice with 1x PBS and DAPI is added for 30 min at room temperature in 1xPBS. Images were acquired with a Zeiss LSM780 confocal microscope keeping laser power same for NHS and HS. The mean intensity per nucleus (DAPI channel) is calculated using Imaris 9.3 in arbitiary units and a background value of 6 is subtracted from each measurement. Data is plotted in Prism 7.

For FACS, similar protocol was followed and DAPI stained cells with NELFA- IF were subjected to analysis using FACS. Briefly, Trypsinized cells were resuspended in complete DMEM and washed with chilled 1X PBS. Then the cells were resuspended in chilled pre-extraction buffer (0.2% Triton X-100 in 1X PBS) and incubated on ice for 4 min. The cells were washed with 1X PBS with 1% w/w BSA and fixed with 4% formaldehyde in 1X PBS for 10 min at RT. For analysis of chromatin retained NELF, pre-extracted cells were measured on a BD LSRFortessa ii flow cytometer (BD Biosciences). Data were analyzed or FlowJo software 9.9.6 (BD).

Chemical treatments

Treatment with the SUMO E1 inhibitor ML-792 (kind gift from UbiQ) was performed at a final concentration of 1 μM for 1 h immediately before induction of heat shock. Similarly CDK9 inhibitor DRB was used at final concentration of 100 μM for 1 h.

RNA interference

SMARTpool siRNA reagent (Dharmacon) was used. This siRNA mix is a pool of four siRNA duplexes designed to target distinct sites within the specific gene of interest, while not to having significant off-target effects based on *in silico* predictions. Cherry-pick libraries from Dharmacon comprising several siRNA SMARTpool and nontargeting controls were ordered. NELFA-3′UTR specific siRNA was ordered from Microsynth as set of three different siRNA duplexed and mixed together to a final stock concentration of 10 μM each. E3 ligase siRNAs (for knockdown of PIAS1, PIAS4 and ZNF451) were ordered from Origene. HeLa cells were plated 24 h prior to transfection. siRNAs were transfected using RNAiMax according to the manufacturer's instructions (Invitrogen, 13778075). siRNAs were transfected at 30 pmol per well of 6 well plate. Cells were further incubated for 48 h before being harvested for analysis. Knockdown efficiency was confirmed by western blotting.

SILAC based Mass-spectrometric analysis of CDK9 interactome and NELFA phosphorylation

Quantitative mass spectrometry was carried out using the SILAC approach (Ong et al., 2002). For the analysis of the CDK9 interactome, Flp-In T-Rex HEK293 cells that stably express C-terminally GFP-tagged CDK9 or GFP, were cultured in normal medium ('light'), medium containing $^{2}H_4$-lysine and $^{13}C_6$-arginine ('medium'), or $^{15}N_2{}^{13}C_6$-lysine and $^{15}N_4{}^{13}C_6$-arginine ('heavy') supplemented with dialyzed FBS (Thermo Fisher Scientific, 88440) for at least five cell divisions (starting density < 1%). Light-, medium- and heavy-labeled cells were then either exposed to heat shock conditions (43°C, 1.5 h) or left at 37°C. Three replicate experiments were conducted following the label-swap strategy (Park et al., 2012). After the treatment, cells were chemically crosslinked using 1% formaldehyde for 10 min and quenched for 5 min using excess L-glycine. Cells were then lysed in 1xRIPA buffer (50 mM Na-HEPES pH 7.4, 150 mM NaCl, 0.5% sodium deoxycholate, 0.1% SDS, 0.1% Triton X-100, 5 mM $MgCl_2$, 10% glycerol) and combined in equal amounts. The cell lysate was sonicated using a BioRuptor system and cleared by centrifugation. The cleared cell lysate was then applied to GFP-trap magnetic agarose beads (ChromoTek, gtma 20) for 1 h at 4°C. Beads were then washed with high salt buffer (50 mM Tris-HCl pH 7.4, 1 M NaCl, 1% NP40, 0.5% sodium deoxycholate, 0.1% SDS, 1 mM EDTA) and non-denaturing buffer (50 mM Tris-HCl pH 7.4, 100 mM NaCl, 0.1% Tween-20). Proteins were digested sequentially on the beads with LysC and then with trypsin in solution. Peptides were desalted and analyzed using a Q-Exactive mass spectrometer (Thermo Fisher Scientific) coupled to an nLC 1000 Nano UHPLC (Thermo Fisher Scientific). Raw files were processed using MaxQuant (version 1.5.7.4) and analyzed using Perseus (version 1.5.2.4). First, decoy and contaminant entries were removed. Next, specific CDK9 interactors were discriminated from background interactors under steady-state and heat shock conditions. For this, Student's t tests were performed based on the iBAQ intensities of proteins quantified in GFP and GFP-CDK9 pulldowns. Proteins exhibiting $\geq$2-fold enrichment and a t test p value $\geq$0.1 were defined as GFP-CDK9 specific interactors in both conditions. Subsequently, SILAC ratios of common CDK9 interactors under steady state and heat shock conditions were extracted and normalized so that the SILAC ratio of CDK9 equals one to account for slight variations in IP efficiency. Simultaneous western blots of the input material were performed to confirm that the intracellular CDK9 level did not change upon heat shock.

CDK9 interactone score was calculated using double ratio normalization method as mentioned below.

CDK9 interactone score (HS/NHS) = SILAC ratio of protein HS/NHS in respective replicate divided by SILAC ratio of CDK9 HS/NHS in same replicate

For analysis of NELFA phosphorylation, Flp-In T-Rex HEK293 T-Rex cells that stably express C-terminally GFP-tagged NELFA were used. All procedures were conducted in triplicates as described above. Three different phosphorylation sites on NELFA were detected in each of the replicates with high confidence (PTM score > 0.99).

Chromatin immunoprecipitation and quantitative PCR(qPCR)

Chromatin immunoprecipitation and qPCR experiments were performed as described previously (Arrigoni et al., 2016). Briefly, cells were fixed using 1% methanol-free formaldehyde (Thermo Scientific, 28906) in DMEM media at room temperature for 10 min, followed by 5 min quenching with 0.125 M glycine. Cells were then washed two times with ice-cold PBS and the cell pellet was resuspended in Farnham buffer (5 mM PIPES, pH 8; 85 mM KCl; 0.5% Igepal). Cell suspensions were sonicated in 1 ml Covaris tubes

(Covaris, 520130) using Covaris S220 with the following settings: peak power = 75; duty factor = 2; cycles/burst = 200. Sonication time varied from cell type to cell type; For HeLa, Sonication time of 4 minutes is used. Isolated nuclei were washed with Farnham buffer and suspended in shearing buffer (10 mM Tris-HCl, pH 8; 0.1% SDS; 1 mM EDTA). Chromatin was sheared by sonication in 1 mL Covaris tubes using the following settings: peak power = 140; duty factor = 5; cycles/burst = 200, time = 45 minutes. These settings led to a DNA fragment–size distribution of 200–600 bp. Debris was removed by centrifugation. Chromatin was then diluted 1:1 with IP buffer (GFP-trap dilution buffer; 10 mM Tris-Cl pH 7.5, 150 mM NaCl, 0.5 mM EDTA) to achieve a final SDS concentration of 0.05%. For immunoprecipitation, GFP beads were incubated overnight at 4°C with 200 μg chromatin. An aliquot of chromatin was saved as input DNA. Beads were washed and DNA–protein complexes were eluted from the beads by heating at 65°C in elution buffer (50 mM Tris-HCl, pH 8.0, 10 mM EDTA and 1% SDS). Crosslinking was reversed for 6 h at 70°C and samples were treated with 200 μg ml^{-1} RNase A (Applichem, A3832) and 200 μg ml^{-1} proteinase K (Sigma-Aldrich, P2308). Immunoprecipitated DNA was purified with phenol–chloroform extraction and ethanol precipitation and used either as input for subsequent qPCR or library preparation for next-generation sequencing. For ChIP-qPCR, enrichment of the immunoprecipitated DNA at the corresponding loci was expressed as a percentage relative to the input DNA.

Quantitative PCR with reverse transcription and nascent-transcript quantification assay

HeLa cells were plated and 24 h post plating, endogenous NELFA was knocked down using Lipofectamine RNAi MAX with concurrent transfection with either NELFA WT or NELFA ΔIDR replacement mutants using Lipofectamine 3000 as per manufacturer's instructions. Media was changed 24 h after transfections. Cells were harvested in trizol 24 h after the change of media (48 h after transfections). RNA was extracted using Trizol as per manufactures protocol. RT reaction was done using Takara PrimeScript RT reaction kit (RR047A) and qPCRs were done using Takara TB Green Premix Ex-Taq (RR420L). Nascent transcripts were detected using intron-exon primer pairs as described (Palozola et al., 2017). cDNA was amplified in a Step One Plus Real-Time PCR system (Applied Biosystems). DNA amounts were quantified using the ΔΔCt method, and the nontreated condition was set to 1. hnRNP was used as normalized consistent with previous study (Aprile-Garcia et al., 2019). The heatmap for qPCRs was generated in Prism 7 using mean values.

In vitro SUMO assays

In vitro SUMOylation assays were performed as reported before (Eisenhardt et al., 2015; Knipscheer et al., 2008; Pichler, 2008; Pichler et al., 2004). Briefly, 20 mM HEPES, pH 7.3, 110 mM potassium acetate, 2 mM magnesium acetate, 0.05% (v/v) Tween20, 0.5 mM TCEP, 0.2 mg/mL ovalbumin and 5 mM ATP reactions buffer was used for 20 μL reaction volumes at 30°C for 30 min. 50nM of E1 and E2, 50 and 150nM of E3, 200 nM Substrate and 2000 nM of SUMO2 enzymes were used for each reaction. Reactions were terminated by boiling with SDS loading buffer and resolved by SDS-PAGE. Detection was done using western blotting using protein specific antibodies.

RNA Pol II ChIP seq library preparation and data analysis

Libraries from Niskanen et al. (2015). Genome Biology 2015 were used for RNA Pol II ChIP sequencing. Libraries were sequenced deeper to detect gene body Pol II signal.

Cell viability assay

Cell viability assay was perfromed using CellTiter-Glo 2 Luminescent Cell Viability Assay (Promega, G7570) accoring to manufacturer's instructions. Briefly, cells were seeded in 96 well cell culture plates at density of 5000 cells per well. Cells were transfected 24 h after seeding with NELFA siRNA specific against 3′UTR and WT, dIDR NELFA or IDR replacement plasmids using their respective transfection reagents as mentioned above. About 24 h after transfection, the medium was exchanged and cells were incubated for another 24 h. Following this, cells were subjected to heat shock at 43°C for different durations (60, 120 and 240 min). After heat shock treatment, cells were recovered at 37°C for 24 h and cell viability assay was performed.

For CDK9, CCNT1 and ZNF451, Cells were transfected 24 h after seeding with NELFA mentioned plasmids using their respective transfection reagents as mentioned above. About 24 h after transfection, cells were subjected to heat shock at 43°C for different durations (180 and 240 min). After heat shock treatment, cells were recovered at 37°C for 24 h and cell viability assay was performed.

Luminiscence readings were taken using microplate luminometer (Centro LB 960 – Berthold technologies) and Mikrowin 2000 software Version 4.41, English UI.

Expression and purification of full-length NELF and tentacle deletion variants

Full-length human NELF complex and variants lacking either the NELFA tentacle (Δ189-528) or NELFE tentacle (Δ139-380) were overexpressed in High Five insect cells (Expression Systems) as previously described (Vos et al., 2018b; Vos et al., 2016).

NELF complex was purified essentially as described (Vos et al., 2018b; Vos et al., 2016). In brief, the cleared lysate was loaded onto a 5 mL HisTrap column (GE healthcare), which was pre-equilibrated in lysis buffer (20 mM Na-HEPES pH 7.4, 300 mM NaCl, 30 mM imidazole, 10% glycerol, 1 mM DTT, 0.284 μg/mL leupeptin, 1.37 μg/mL pepstatin A, 0.17 mg/mL PMSF, 0.33 mg/mL benzamidine) and then washed with high salt buffer (20 mM Na-HEPES pH 7.4, 800 mM NaCl, 30 mM imidazole, 10% glycerol, 1 mM DTT, 0.284 μg/mL leupeptin, 1.37 μg/mL pepstatin A, 0.17 mg/mL PMSF, 0.33 mg/mL benzamidine). After re-equilibration in lysis buffer,

the column was washed with low salt buffer (20 mM Na-HEPES pH 7.4, 150 mM NaCl, 30 mM imidazole, 10% glycerol, 1 mM DTT, 0.284 μg/mL leupeptin, 1.37 μg/mL pepstatin A, 0.17 mg/mL PMSF, 0.33 mg/mL benzamidine) and attached in-line to a 5 mL HiTrap Q column (GE healthcare) equilibrated in low salt buffer. The protein was eluted then using elution buffer (20 mM Na-HEPES pH 7.4, 150 mM NaCl, 500 mM imidazole, 10% glycerol, 1 mM DTT, 0.284 μg/mL leupeptin, 1.37 μg/mL pepstatin A, 0.17 mg/mL PMSF, 0.33 mg/mL benzamidine). Appropriate elution fractions were mixed with 6xHis-tagged TEV protease and Lambda protein phosphatase and dialyzed overnight against lysis buffer containing 1 mM $MnCl_2$. To remove the 6xHis tag and TEV protease, the dialysate was applied to a 5 mL HisTrap column equilibrated in lysis buffer. The flow through was concentrated using a 100 kDa MWCO Amicon spin filter (Merck) and subjected to gel filtration using a HiLoad 16/600 Superdex 200 pg column (GE healthcare) in NELF size-exclusion buffer (20 mM Na-HEPES pH 7.4, 150 mM NaCl, 10% glycerol, 1 mM DTT). To produce P-TEFb pretreated NELF, an aliquot was removed and incubated with 0.4 μM gluthathione S-transferase (GST)-tagged P-TEFb, 6 mM $MgCl_2$, and 3 mM ATP for 2 h at 30°C. GST-tagged P-TEFb was bound to pre-equilibrated GSTrap 4B resin (GE healthcare) and the NELF-containing supernatant was subjected again to size-exclusion chromatography on a HiLoad 16/600 Superdex 200 pg column. Appropriate fractions were pooled, concentrated, and aliquots were flash-frozen and stored at –80°C.

Expression and purification of GFP-NELF tentacle fusion proteins

The sequence encoding either the tentacle regions of NELFA (residues 189-528) or NELFE (residues 139-380) was cloned C-terminal of a 6xHis-tagged monomeric (A206K) enhanced green fluorescent protein (EGFP)-tag followed by a tobacco etch virus (TEV) protease cleavage site into a modified, pET-derived vector (Addgene, 29654) using Gibson assembly (New England Biolabs). Both plasmids were used as template to generate a double tentacle GFP fusion protein construct with a TEV protease-cleavable 6xHis-tag followed by the NELFE tentacle sequence at its N terminus and the NELFA tentacle sequence at its C terminus. NELF tentacle-GFP fusion proteins were overexpressed in *E. coli* BL21 (DE3) cells (Agilent). Overexpression was induced by the addition of 0.5 mM isopropyl β-d-1-thiogalactopyranoside (IPTG) after the culture reached an optical density at 600 nm of ~0.8. The cells were cultured for further 3-4 h at 22°C, harvested by centrifugation, resuspended in lysis buffer (20 mM Na-HEPES pH 7.4, 300 mM NaCl, 30 mM imidazole, 10% glycerol, 1 mM DTT, 0.284 μg/mL leupeptin, 1.37 μg/mL pepstatin A, 0.17 mg/mL PMSF, 0.33 mg/mL benzamidine), flash-frozen and stored at −80°C until purification.

For purification of NELF tentacle GFP fusion proteins, lysate was loaded on a 5 mL HisTrap column pre-equilibrated in lysis buffer. The column was washed with high salt buffer (20 mM HEPES pH 7.4, 1 M NaCl, 10% glycerol, 1 mM DTT, 0.284 μg/mL leupeptin, 1.37 μg/mL pepstatin A, 0.17 mg/mL PMSF, 0.33 mg/mL benzamidine) and eluted in a linear 20CV gradient with elution buffer (20 mM Na-HEPES pH 7.4, 300 mM NaCl, 500 mM imidazole, 10% glycerol, 1 mM DTT, 0.284 μg/mL leupeptin, 1.37 μg/mL pepstatin A, 0.17 mg/mL PMSF, 0.33 mg/mL benzamidine). Appropriate pure fractions were pooled. Single NELF tentacle-GFP fusion proteins were concentrated with a 30 kDa MWCO Amicon Ultra centrifugal filter and then loaded onto a Superdex 200 10/300 Increase column preequilibrated in NELF size-exclusion buffer (20 mM Na-HEPES pH 7.4, 150 mM NaCl, 10% glycerol, 1 mM DTT). Appropriate fractions containing the NELF double tentacle-GFP fusion protein were mixed with 6xHis-tagged TEV protease to cleave the hexahistidine tag during overnight dialysis against lysis buffer. The protein was then loaded on a 5 mL HisTrap column pre-equilibrated in lysis buffer. Flow through fractions were collected and concentrated with a 30 kDa MWCO Amicon Ultra spin filter. The concentrated protein solution was then applied onto a Superdex 200 10/300 Increase column pre-equilibrated in NELF size exclusion buffer (20 mM HEPES pH 7.4, 150 mM NaCl, 10% glycerol, 1 mM DTT). Peak fractions were pooled, concentrated, and aliquots were flash-frozen in liquid nitrogen and stored at −80°C.

Expression and purification of P-TEFb

Active P-TEFb (CDK9 1–372, CYCT1 1–272) and the catalytically inactive P-TEFb variant (containing the D149N substitution in CDK9) were expressed in High Five insect cells and purified as previously described (Vos et al., 2018a; Vos et al., 2018b).

Fluorescent labeling of NELF complex

NELF complex was incubated with a 10-fold molar excess of fluorescent TFP-Alexa Fluor 488 dye (Molecular Probes) for 1 h on ice in the dark. The reaction was quenched by addition of L-lysine (in 50 mM Tris-HCl pH 7.0) in a 10-fold molar excess to the dye. The reaction was then desalted using a Micro Bio-Spin P6 gel column (Biorad) pre-equilibrated in NELF size-exclusion buffer according to the manufacturer's instructions, followed by multiple diafiltration steps using a 30 kDa MWCO Amicon spin filter (Merck). After concentration, small aliquots were flash-frozen and stored at −80°C. The protocol resulted in a low labeling density of ~1.0-1.2 fluorophores per NELF molecule.

In vitro phase separation assays and microscopy

Phase separation assays were conducted in modified 50-well CultureWell chambered coverslides (Grace Bio-Labs). To minimize nonspecific adsorption, the coverslide was passivated with methoxy poly(ethylen glycol) (mPEG) silane, following a similar procedure as described (Gibson et al., 2019). For this, the coverslides were washed with 2% Hellmanex III solution (Hellma Analytics) for 2 h and rinsed with ultrapure water. The glass surface was etched with 1 M NaOH for 1 h, washed with ultrapure water and incubated overnight with mPEG silane with an average molecular weight of 5 kDa (25 mg/mL in 95% EtOH; Nanosoft Polymers). The glass slide was subsequently rinsed with ultrapure water, dried and sealed with crystal clear tape.

For phase separation assays with the NELF complex, unlabeled and Alexa Fluor 488-labeled protein were mixed at a molar ratio of 9:1. NELF complex or GFP fusion protein solutions were generally diluted to the indicated final concentrations in 20 mM Na-HEPES, pH 7.4, 50 mM NaCl, 10% glycerol, 1 mM DTT in a total volume of 5.1 μl to induce phase separation. To test sensitivity of LLPS toward aliphatic alcohols, 1,6-hexanediol (Sigma Aldrich) was included at a final concentration of 10%. The plate was sealed with crystal clear tape to minimize sample evaporation and incubated for 1-2 h in the dark to allow formed droplets to settle down on the coverslide surface. Images were acquired above the coverslide surface using an inverted Leica TCS SP8 laser scanning confocal microscope with a HC PL APO 63x/1.40 CS2 objective (oil immersion) at room temperature (22 ± 1°C). Generally, at least 5 images per condition were taken in non-overlapping regions, which were considered representative for the droplet distribution on the slide. Images were further processed and analyzed using FIJI (version 1.52 h).

In vitro FRAP experiments

Fluorescence recovery after photobleaching (FRAP) was used to determine the effect of P-TEFb phosphorylation on the mobility of molecules in the condensed phase. Dephosphorylated as well as P-TEFb-treated NELF were diluted to 2 μM (partial droplet FRAP experiments) or 2.5 μM (full droplet FRAP experiments) in 20 mM Na-HEPES pH 7.4, 50 mM NaCl, 10% glycerol, 1 mM DTT to induce LLPS. Afterward, the plate was incubated for around 1 h in the dark prior to imaging. FRAP movies were recorded at a resolution of 256 × 256 pixels with a pixel size of 96 × 96 nm. The 488 nm argon laser line was used at full laser intensity to photobleach a defined region of interest to ~10%–20% of its initial fluorescence. For partial droplet bleaching, a 1 μm circular region was bleached within the center of droplets with a diameter of around 6.0-7.5 μm. Fluorescence recovery was imaged every 0.5 s over a period of 250 s. For full droplet FRAP, the entire area of droplets with a diameter of around 5-6 μm was photobleached and 600 frames were recorded with a frame rate of 0.5 s^{-1}. Fluorescence recovery of the bleached region was analyzed using FIJI (version 1.52 h). For this, the fluorescence intensity of the bleached spots was background subtracted, normalized to the fluorescence intensity of the first postbleach image, corrected for acquisition bleaching using a similarly-sized reference droplet in the frame, and normalized to the mean prebleach intensity. The obtained recovery curves were fit to a double-exponential recovery model using Prism (GraphPad software, version 5.03).

Real-time P-TEFb droplet phosphorylation

For droplet phosphorylation experiments with P-TEFb, Alexa Fluor 488-labeled and unlabeled NELF complex were mixed at a molar ratio of 1:9 and diluted to a final concentration of 1 μM in 20 mM Na-HEPES, pH 7.4, 50 mM NaCl, 10% glycerol, 1 mM DTT, 1.5 mM ATP and 4.5 mM $MgCl_2$. The microscopy slide was then sealed and incubated on the microscope stage for 2 h in the dark to allow NELF droplets to settle down quantitatively on the coverslide surface. Subsequently, either active P-TEFb or a catalytically inactive P-TEFb variant (containing the D149N substitution in CDK9) were added gently to a final concentration of 0.2 μM. Immediately after P-TEFb addition, a series of images was acquired in a representative area and imaged in regular intervals for 120 min.

Mass spectrometric analysis of P-TEFb phosphorylation sites

Dephosphorylated and P-TEFb-treated NELF samples were separated on a SDS-PAGE gel, respective bands were subjected to tryptic in-gel digestion, and the obtained peptide mixture was enriched for phosphopeptides as described previously (Oellerich et al., 2009). After desalting, the peptide mixture was analyzed using a Q-Exactive HF mass spectrometer (Thermo Fisher Scientific) coupled to a Dionex UltiMate 3000 nano liquid-chromatography system (Thermo Fisher Scientific) (Oellerich et al., 2009). The raw files were processed using MaxQuant (version 1.5.2.8) (Cox and Mann, 2008). The data were searched against the human Uniprot proteome database using default settings, except that serine, threonine, and tyrosine phosphorylation, methionine oxidation, and carbamidomethylation of cysteine were allowed as variable modifications. Identified phosphorylation sites were filtered for high confidence with a posttranslational modification (PTM) score > 0.75. All reported sites were detected exclusively in the P-TEFb-treated NELF sample.

Analysis of NELF-CTD interaction

To test whether NELF droplets interact with the RNA polymerase II CTD, we analyzed partitioning of different CTD fusion proteins. 6xHis-tagged maltose-binding protein (MBP) fusion proteins with the full-length human CTD (residues 1593-1970) (Boehning et al., 2018), the full-length *S. cerevisiae* CTD (residues 1542-1733) (Boehning et al., 2018) as well as the distal half of the human CTD (1776-1970) were expressed in *E. coli* and purified to homogeneity as described previously (Boehning et al., 2018). The proteins possess a single cysteine residue C-terminal of a TEV protease cleavage site that was used for site-specific labeling with an Alexa Fluor (AF) 647 C2 maleimide (Invitrogen, A20347). AF647-labeled CTD fusion proteins in NELF150 buffer (20 mM Na-HEPES pH 7.4, 150 mM NaCl, 10% glycerol, 1 mM DTT) were mixed with AF488-labeled NELF complex and 6xHis-tagged TEV protease, prior to induction of LLPS, resulting in final protein concentrations of 2.5 μM NELF, 2 μM MBP-CTD fusion protein and 0.25 μM TEV protease. The reaction was incubated for 1 h in the dark at room temperature to allow for TEV cleavage and droplets to settle, prior to imaging using a Leica SP8 microscope in sequential scanning mode.

To investigate the effect of different CTD phosphorylation marks on the interaction with NELF condensates, we analyzed the partitioning of synthetic CTD peptides between the condensed and dilute NELF phase. For this, N-terminally carboxyfluorescein (FAM)-labeled CTD peptides with the sequence SPSYSPTSPSYSPTSPS that possess phosphoryl groups at the indicated heptad positions

(PSL GmbH) were mixed with unlabeled NELF complex, prior to induction of LLPS, leading to final concentrations of 2.5 μM NELF and 1 μM of the respective peptide. The plate was incubated and imaged as described above. For the calculation of partition coefficients, the recorded images were segmented into condensed and dilute phase using brightfield images and peptide partitioning was analyzed based on the peptide fluorescence within dilute and condensed phase. For this, the fluorescence intensity was determined and averaged for three regions of interest within the condensed and dilute phase of each image. Determined fluorescence intensities for condensed and dilute phase were background-subtracted by the fluorescence intensity of a sample lacking CTD peptide. The corrected fluorescence intensities of the condensed phase were divided by the corrected intensity of the dilute phase to calculate the partition coefficients. For each peptide, partition coefficients were calculated as the ratio of the background-subtracted fluorescence intensities within and outside of the condensed phase for n = 12 different recorded images.

SLAM-Seq Experiments

HeLa cells were plated, and after 24 h for experiment (1) NELFA Wildtype was knocked down using Lipofectamine RNAi MAX with concurrent transfection with either NELFA WT or NELFA ΔIDR using Lipofectamine 3000, for experiment (2) scrambled siRNA and siZNF451 was used with Lipofectamine RNAi MAX all per manufacturer's instructions. Media was changed 24 h after transfection and/or knockdown. Heat-shock and labeling was carried out 24 h after the change of media (48 h after transfection and/or knockdown) in the following manner:

For NELFA WT and NELFA-ΔIDR experiment - Cells were subject to heat shock at 43°C for 60 min, with labeling beginning at the start of heat-shock with 200 μM 4SU (Cayman Chemical 16373). The total labeling time was 60 min.

For siZNF451 experiment - Cells were subject to heat shock at 43°C for 30 min, with labeling beginning 15 min into heat-shock with 200 μM 4SU (Cayman Chemical 16373), after a total of thirty minutes of heat-shock, cells were returned to 37°C for 90 min of recovery. The total labeling time was 105 min.

RNA was extracted using Trizol per manufactures protocol, with addition of DTT to a final concentration of 1mM, and protected from light during the procedure to prevent S-S cross-binding. 5μg of RNA was used for SLAM-seq modifications, as described in (Herzog et al., 2017). Briefly, Iodoacetamide (Sigma I1149) was conjugated to 4SU in a 50mM pH 8.0 phosphate buffer in DMSO/Water (1:1), the reaction was quenched with DTT and RNA was reprecipitated using Ethanol and NaOAc. Libraries were prepared using Quantseq 3′ mRNA-Seq Library Prep Kit (Lexogen).

Bioinformatic analysis

ChIP-seq reads were aligned to the human genome build hg38 using Bowtie2 (Langmead and Salzberg, 2012). Duplicate and discordant reads were removed. Peak calling was done with MACS2 (Zhang et al., 2008) (model- based analysis of ChIP- Seq) using "–keep-dup all," "–nomodel," "–extsize" and "–broad." Gene annotations and transcript start site (TSS) information for human genes were from taken from Gencode annotation release 26. Genes considered for differential gene body rpkm analysis were filtered similar to Chen et al. (2015): the rpm of the TSS region (from the TSS to 500 bp downstream of the TSS) had to be at least 1, genes had to be longer than 2kb and more than 1kb distant to any neighboring gene. In case a gene had several TSSs, the highest occupied (based on rpm) was taken. Gene body was defined for the remaining genes as TSS + 1500bp to transcription end site (TES) – 500bp. Reads overlapping the gene body regions were counted using bedtools 10. Differential analysis of gene body density was done using DESeq2 (Love et al., 2014). Size factors were calculated based on the ChIP-seq signal of very long genes as proposed by Mahat et al. (2016). MAplots of differential gene body density were visualized using ggplots2 (Wickham, 2016) package in R with signifcant genes (padj < 0.1) highlighted in red.

For visualization, the paired-end reads were extended to fragment size and normalized to total reads aligned (reads per million, rpm) using deeptools2 (Ramirez et al., 2016). All browser tracks were visualized using Integrative Genome Viewer (http://software.broadinstitute.org/software/igv/). Profile Plots for TSS regions (TSS+/− 500bp) and gene body regions were generated using deeptools2. Violin plots were generated with the vioplot package in R using the log2 fold change of the gene body counts. Only top 250 expressed genes (based on Pol II density at TSS in NHS samples) were used for visualization.

Boxplots depicting the ratio of NELFA/E ChIP-seq signal increase upon HS over the ratio of Pol II ChIP-seq signal increase were plotted using ggplot2 (Wickham, 2016). Significance was calculated using Wilcoxon rank sum test.

Histograms showing the NelfA/E ChIP-seq signal increase upon HS of significantly downregulated genes and NELF target genes with their corresponding gene body density misregulation upon HS, respectively, were plotted using gplots (Warnes, 2012). NELF target genes were defined as genes with a ChIP-seq signal in the TSS region (TSS+/−250bp) > 2 rpm.

SLAM-seq analysis was done similar to Neumann et al. (2019). 3′UTR annotations were taken from Gencode annotation release 31 and merged on a gene level. Adapters and polyA stretches were trimmed from raw reads using fastp (Chen et al., 2018). Trimmed reads were further processed with SlamDunk v0.3.4 16. "Slamdunk all" command was executed with default parameters except '-5 12 -n 100 -t 20 –m -rl 100–skip-sam'.

Differential gene expression was done with DESeq2 using raw read counts with at least 2 T>C conversions. MAplots of differential gene expression were visualized using ggplots2 (Wickham, 2016) package in R with signifcant genes (padj < 0.1) highlighted in red. Size factors were calculated based on corresponding total read counts for global normalization.

Violin plots were generated with the vioplot package in R using the log2 fold change based on reads with > = 2 T>C conversions. Only genes with a padj < 0.1 were used for visualization. The same gene lists were plotted as a heatmap using ComplexHeatmap package in R (Gu et al., 2016).

Scatterplots of log2FoldChanges upon different conditions were generated using gplots (Warnes, 2012).

Pairwise correlation scatterplots by replicates were plotted using ggplot2 (Wickham, 2016) using spearman correlation method.

Go analysis was done using Metascape (Zhou et al., 2019) with Express analysis and pathways enriched with –log10(P) vlaue of more than or equal to 10 are represented in manuscript.

QUANTIFICATION AND STATISTICAL ANALYSIS

All the statistical analysis is done using GraphPad – Prism Version 7. The statistical details can be found in the figure legends of corresponding experiments and Method details section.